remote sensing

MDPI

Article

Seasonal Varied Responses of Block-Scale Land Surface Temperature to Multidimensional Urban Canopy Morphology Interpreted by SHAP Approach

Xinxin Luo [1], Jiahao Wu [2,3], Wentao Peng [1], Minghan Xu [1], Fengxiang Guo [4] and Die Hu [1,*]

[1] School of Earth Sciences and Resources, China University of Geosciences (Beijing), Beijing 100083, China; 2001240149@email.cugb.edu.cn (X.L.); 2101240082@email.cugb.edu.cn (W.P.); 2001240148@email.cugb.edu.cn (M.X.)
[2] Aerospace Information Research Institute, Chinese Academy of Sciences, Beijing 100094, China; wujh@aircas.ac.cn
[3] State Key Laboratory of Internet of Things for Smart City, Department of Ocean Science and Technology, University of Macau, Macao 999078, China
[4] Department of Geography, The University of Hong Kong, Hong Kong 999077, China; guofx@hku.hk
* Correspondence: hudie@radi.ac.cn

Highlights

What are the main findings?

- A composite morphological block (CMB) zoning scheme for thermal characterization.
- Factors related to the artificial landscape are the dominant driver of LST during the warm months. 2D and 3D vegetation canopy morphology contributed more to LST in the cold months.

What are the implications of the main findings?

- CMBs can more accurately classify and analyze the temperature at the block scale.
- The impact analysis based on 2D and 3D urban factors can be more reliable to evaluate the contribution degree.

Abstract

Rising urban temperatures have become a critical constraint to urban ecosystem resilience and livability due to rapid urbanization. This study proposes a novel intra-city zoning scheme, named component morphological blocks (CMBs), which classifies built-up areas into six types characterized by multidimensional urban canopy morphologies. The XGBoost-SHAP model, optimized via Bayesian tuning, was employed to examine the relative contributions of 16 potential driving variables to block-scale land surface temperature (LST). The results show that: (1) LST gradually increases with increasing building density in the warm seasons. The average building height (BH) exhibits a positive correlation with shaded area, thereby reducing LST on the block scale; (2) hotspots are mainly concentrated in function-oriented blocks with hotspot distribution indices of 1.85, 1.96, 1.24, and 1.14, respectively. Coldspots are largely observed in blue–green space in the warm seasons; (3) BH dominates the LST across seasons, while the building-related factors make a prominent impact on LST in warm seasons. The contribution of vegetation canopy density is followed by BH during autumn and winter (12.2%, 10.9%); (4) a distinct transition occurs between summer normalized difference built-up index (NDBI) and fractional vegetation cover around an NDBI of 0.1. In winter, the interaction between 2D and 3D vegetation factors indicates a shift in their relative contributions from negative to positive as they increase. This study demonstrates that CMBs serve as an effective choice for characterizing

Check for updates

Academic Editor: Pinliang Dong

Received: 9 February 2026
Revised: 18 March 2026
Accepted: 24 March 2026
Published: 27 March 2026

Copyright: © 2026 by the authors. Licensee MDPI, Basel, Switzerland. This article is an open access article distributed under the terms and conditions of the Creative Commons Attribution (CC BY) license.

LST patterns at the block scale, providing insights for sustainable urban development aimed at mitigating the urban heat island effect.

Keywords: urban morphology; spatiotemporal pattern; urban remote sensing; XGBoost-SHAP model; land surface temperature

1. Introduction

In response to the multiple challenges posed by global climate change and rapid urbanization, the United Nations has established Sustainable Development Goal 11 (SDG 11), which focuses on building inclusive, safe, resilient, and sustainable cities and communities [1]. SDG 11 emphasizes strengthening national and regional development planning to foster positive economic, social, and environmental connections between urban, peri-urban, and rural areas. In this context, the continuous expansion of impervious surfaces reduces the cooling effects of vegetation and wetlands, leading urban areas to experience higher air/surface temperatures than their rural surroundings, a phenomenon generally referred to as the urban heat island (UHI)/surface urban heat island (SUHI) effect [2]. Notably, China's urbanization rate is projected to exceed 67% by the end of 2024 (Statistical Bulletin on National Economic and Social Development of the People's Republic of China, 2024–2025). Excessive urbanization poses severe challenges to urban ecological stability and the well-being of urban residents [3]. The urban canopy layer (UCL) is contained within the lower portion of the urban roughness sublayer and is specifically defined as the layer below the height of major urban elements [4]. The urban canopy profoundly shapes the evolution of local climate characteristics and thermal environment patterns by influencing the energy balance and water cycling at the near-surface–atmosphere interface [5]. Therefore, effectively detecting the relationship between the urban thermal environment and multidimensional canopy morphology has become a significant topic in the field of relevant research [6].

In recent years, multiplatform remote sensing (RS) sensors have provided accessible high-resolution urban morphology products and land surface temperature (LST) data, which has become the primary data source for multiscale SUHI investigations [5]. For instance, LiDAR and street-view imagery have been extensively applied to construct tree canopy models for extracting detailed canopy parameters [7]. Regarding quantitative thermal evaluations, investigators commonly adopt air temperature (AT) or LST as prevalent indicators [8]. RS-derived LSTs cover a wide spatial range and serve as a critical regulator of near-surface air temperature, which is also a core element of the radiation balance and energy exchange [4]. Consequently, LST is a key indicator used in remote sensing research to characterize urban surface heat conditions. It is also one of the primary datasets for analyzing the spatial heterogeneity of the surface thermal environment [9].

High-resolution urban canopy data products advance fine-scale urban environmental assessments, especially at the block level [10]. Existing zoning strategies are widely used to describe the surface thermal characteristics represented by LST [11–13]. Specifically, local climate zones (LCZs), delineated on the basis of urban building geometries, land cover types, and surface energy characteristics, improve the precision of urban planning interpretations [14]. LCZs provide a globally standardized typology for urban form and function [15]. However, the rule-based and classification-based nature of these approaches may limit their flexibility when applied to highly heterogeneous urban structures or dynamic urban datasets [16]. Urban functional zones represent the diversity of human activities within municipalities [17]. Numerous studies have examined the relationship between urban blocks and LST under the UFZ framework [18]. Consequently, both LCZ and UFZ schemes have

proven effective for urban zoning and for characterizing spatial thermal patterns [19,20]. In recent years, research on the relationship between urban form and LST has gradually expanded from traditional land cover analysis to two- and three-dimensional urban form indicators [21]. Previous studies have shown that a high proportion of impervious surfaces and intensive development typically lead to increased LST, while higher vegetation cover and water body proportions help reduce LST [22,23]. In addition to compositional characteristics, the two-dimensional landscape pattern itself also influences the thermal environment [24]. Relevant studies show that building density, average building height, and building shadows often influence LST [25]. In addition to buildings, the three-dimensional characteristics of vegetation have also garnered attention. Parameters such as tree height and canopy density, in particular, can exert a significant moderating effect on the urban thermal environment by enhancing shading, evaporative cooling, and improving near-surface energy exchange processes [26]. Previous studies have shown that taller, structurally intact tree canopies typically possess greater potential for daytime surface cooling [27]. The mechanisms underlying this effect primarily involve promoting the release of latent heat through enhanced evapotranspiration, thereby mitigating local heat exposure levels [28]. Furthermore, the vertical stratification of vegetation and its spatial continuity influence near-surface airflow and heat transfer efficiency, resulting in significantly differentiated thermal regulation effects of three-dimensional vegetation structures across different urban spatial units [29,30]. However, the impact of three-dimensional vegetation morphology on LST is not a simple linear process [27]. Its intensity and direction are often jointly constrained by building density, street-valley geometry, background climate, and land surface type [31,32]. Particularly in high-density built-up areas, analyzing LST responses based solely on vegetation cover or building morphology, while ignoring the spatial coupling between buildings and vegetation, may fail to fully reveal the actual mechanisms by which composite canopy structures influence the urban thermal environment. Based on this research, our study considers the integration of multidimensional canopy morphology into the urban block framework. This method extends the scope of traditional two-dimensional (2D) and three-dimensional (3D) characterizations by incorporating vegetation structure as a functional thermal regulation factor within built-up areas [33]. Since urban green spaces play a vital role in mitigating high temperatures, their cooling effect depends on the height and diameter of tree canopies, vegetation density, and related factors [34]. Urban canopy structures thus constitute a set of attributes within the urban spatial system [35]. This study integrates 2D and 3D indicators of urban space. Specifically, we propose a composite morphological block (CMB) framework. Based on this framework, the study examines the extent to which the 2D, 3D, spectral, and functional dimensions of urban form influence LST.

On the temporal scale, multidimensional urban canopy morphological factors exert nonlinear influences on LST, exhibiting varying patterns across seasonal transitions [36]. Numerous methods have been applied to explore the complex mechanisms driving LST, including linear regression analysis [34], stepwise multiple linear regression [37], ordinary least squares [38], Pearson correlation coefficient [39], and geographically weighted regression [40]. However, such approaches are largely based on linear assumptions, are prone to covariance among variables, or struggle to identify interaction effects between potential factors. Subsequently, machine learning models such as elastic networks and random forests [41], along with the Deep Urban Modeller [42], were introduced to enhance their performance in addressing nonlinear relationships. These models are characterized by high computational resource demands, strict data requirements, and limited interpretability [43]. When addressing challenges associated with massive spatio-temporal data processing, XGBoost demonstrates outstanding performance as an efficient gradient boosting algorithm [44]. Existing research indicates that XGBoost performs excellently

in studies involving urban configuration and LST patterns. This is because the model possesses robust predictive capabilities and high computational efficiency [45]. On the other hand, compared with physical models based on surface process modeling, machine learning techniques are often regarded as "black boxes" [46]. This poses significant challenges for understanding the internal decision-making processes of these models [47]. To address this issue, the Shapley Additive Explanations (SHAP) framework enhances the reliability of XGBoost by quantifying the contribution of each feature to prediction outcomes. This approach enhances both global and local interpretability [45]. Given the time cost associated with parameter tuning, this study employs Bayesian methods to optimize the XGBoost–SHAP model [48]. Furthermore, prior models have shown limited ability to capture seasonal nonlinearity or block-scale heterogeneity [49]. Therefore, this study proposes a Bayesian-optimized XGBoost–SHAP model for estimating the nonlinear response of LST to multidimensional morphological factors at the block scale. This framework is particularly suitable for handling seasonal variations driven by multiple interacting factors.

In summary, by relying on high-resolution RS imagery and multisource geographic data, this study aims to comprehensively investigate the coupling relationship between the block-scale thermal environment and urban canopy morphology. The block-scale spatial analysis, combined with machine learning models, reveals the relative contributions, interactions, and marginal effects of 16 driving factors on LST. Three research questions addressed in this study can be summarized as follows:

(1) How to design a flexible block zoning scheme that depicts the integrated two- and three-dimensional morphologies of architecture and vegetation?
(2) What LST patterns do these blocks (i.e., CMBs) exhibit across different seasons?
(3) How do multidimensional factors drive LST through nonlinear interactions?

Taking the megacity of Beijing as an exploratory study case, this research improves understanding of the interactions between urban configuration and thermal environmental patterns. It provides more flexible block zoning schemes (i.e., CMBs) for urban evaluation at finer spatial scales, thereby offering theoretical and technical support for more targeted urban management.

2. Study Area and Data

2.1. Study Area

As mentioned in the Beijing Climate Change Adaptation Action Plan, Beijing is classified as a climate-vulnerable region due to its status as a densely populated, built-up, and landscaped metropolis. Situated in the North China Plain, Beijing (39°28′N to 41°05′N, 115°20′E to 117°30′E) serves as the capital of China (Figure 1). Beijing has a temperate monsoon climate. The population of Beijing increased to 21.832 million in 2020 (Seventh Census, https://tjj.beijing.gov.cn (accessed on 4 August 2025)), with an urbanization rate of 88.2%, making it one of the top ten megacities in the world (https://www.bai.gov.cn (accessed on 4 August 2025)). The study area includes seven districts: Chaoyang, Haidian, Dongcheng, Xicheng, Shijingshan, Fengtai, and Daxing District, with a complex and diverse spatial structure of blocks.

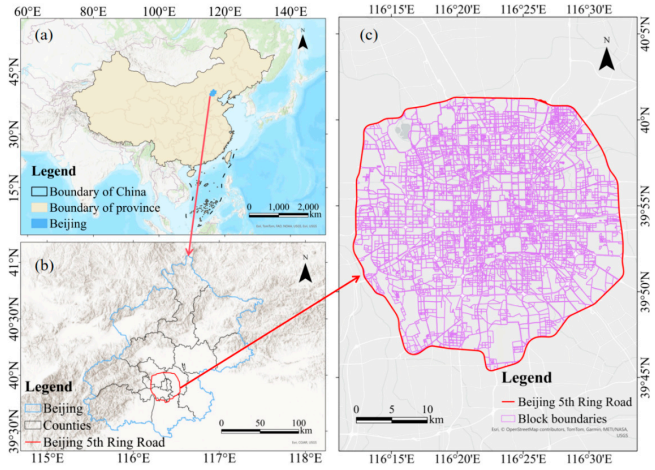


Figure 1. Study area. location of Beijing (**a**). Beijing Fifth Ring Road (**b**). Urban blocks within Fifth Ring Road (**c**).

2.2. Data Sources and Preprocessing

This research provides an overview of the main datasets used which were projected into the WGS_1984_UTM_Zone_50N coordinate system (Table A1). Vegetation canopy data (https://github.com/Jiahao-WW/3Dvegetation-mt2unetplus (accessed on 4 August 2025)), with a resolution of 1 m, were produced with field measurements of tree heights from Gaofen-7 stereo satellite data and handheld laser rangefinders. The data was generated using a multitask convolutional neural network model, and the root mean square error (RMSE) is 3.16 m [50]. The vegetation canopy height data source was generated by integrating multiple Gaofen-7 satellite images captured between 2020 and 2021. Given that Beijing's primary vegetation type is deciduous broadleaf forest, we selected as many spring and summer images as possible. The model's generalization capability was further validated through variations in illumination and seasonal changes across different time periods, generating a 1 m resolution vegetation height map covering the entire urban area of Beijing. The 1 m vegetation canopy height data used in this study is a localized product derived from high-resolution stereoscopic observations by GF-7, primarily intended to characterize the vertical structure of vegetation at the block scale. Height data of buildings was provided [51], which utilized fusion of 0.3–1 m resolution Google Earth imagery, street view images and POI data. It is generated by machine learning and large-scale multimodal models such as OCRNet and XGBoost, which were verified by model benchmark testing and other methods to achieve 80% or more of the results meeting the standard. Street block delineation data (https://figshare.com/articles/dataset/MSDCW_Dataset_and_Code/26021314 (accessed on 4 August 2025)) was based on road data from OpenStreetMap (OSM) and the database of Global Administrative Areas (GADM). This data employs indicators such as the coefficient of variation in area and shape index and they are compared with official data [52]. The study utilizes block parcel data to calculate relevant morphological indicators discussed in the paper, such as floor area ratio and coverage density.

Landsat 8 Thermal Infrared Spectrometer (TIRS) data were utilized for LST calculation, with seasonal data from all four seasons sourced from the Google Earth Engine (GEE) platform [53]. The Landsat 8 image revisit period is 16 days, and spatial resolution in multispectral and thermal infrared bands is 30 m and 100 m, respectively. In this study, four Landsat 8 TIRS images (level 2 products) were selected. When selecting LST data, we prioritize images that, based on data comparison, exhibit low cloud cover, no significant cloud shadow contamination, complete spatial coverage, and are capable of accurately representing seasonal background conditions. Seasonal LST and corresponding spectral indices were extracted from OLI imagery that corresponds to the same season and phase as

the Landsat 8 TIRS imagery to ensure the synchrony of thermal and spectral characteristics on a seasonal scale. Regarding structural indicators such as vegetation canopy height, building height, impervious surface density, and block morphology, given that these factors exhibit relatively limited variation over a one-year timescale within the mature built-up areas inside Beijing's Fifth Ring Road, this study treats them as short-term stable background variables to explain spatial variations in seasonal LST. Point and area of interest datasets which were mainly used to label specific locations and express area-like geographic entities in the map were obtained from OSM maps. AOI types include parks, forests, residential areas, shrublands, nature reserves, etc. (https://www.openstreetmap.org (accessed on 4 August 2025)). POI types include coffee shops, fast-food restaurants, hospitals, schools, banks, etc. (https://www.openstreetmap.org (accessed on 4 August 2025)). Morphological data exhibits slow annual variation. Based on the data sources, vegetation data was acquired from Gaofen-7 imagery, while LST data was obtained from Landsat 8. These data were obtained from GEE. These data have already undergone standard radiometric calibration and atmospheric correction. In this study, we performed additional quality control on this basis and masked out pixels affected by cloud cover (cloud cover < 5%) and other low-quality pixels, ultimately generating the dataset used in this study. When conducting analyses of LST and its influencing factors, the resolution was standardized to 30 m through resampling to ensure spatial consistency [54]. For details on the data sources, please refer to Appendix A.1.

3. Methods

3.1. Research Framework

The structure of this research consists of three distinct sections. First, spatial clustering of CMBs was generated with K-means. Second, the spatial distribution pattern of LST was analyzed. Finally, the driving mechanism of LST was explored from four hierarchies (Figure 2).

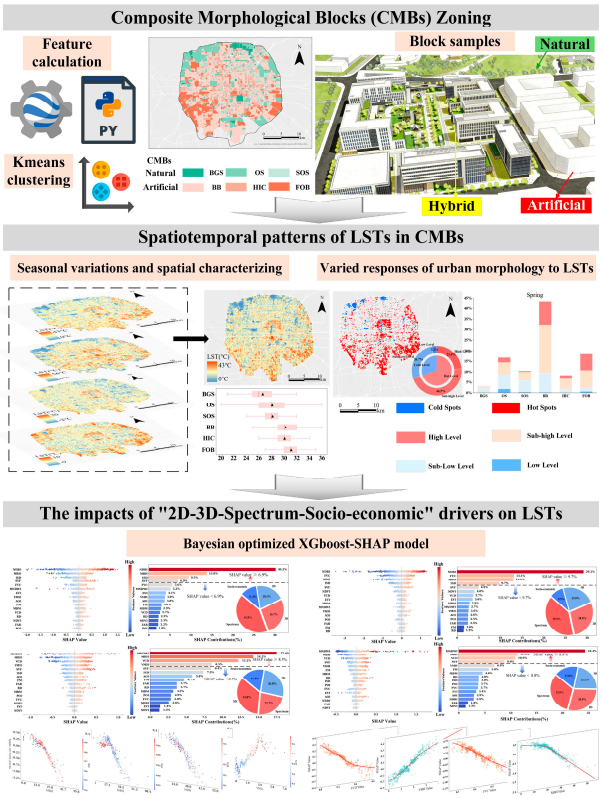


Figure 2. Research framework (Semi-open Space (SOS), High-rise Impervious Core (HIC), Function-oriented Blocks (FOB), Blue–Green Space (BGS), Balanced Built–Green Blocks (BB) and Open Space (OS)).

3.2. Flexible Zoning Approach Based on Unsupervised Clustering

Before clustering, principal component analysis was used to simplify the data by reducing its dimensionality. The first two principal components with scores of 0.73 and 0.23 were retained to cover the main information of source data. The principal components generated by PCA are orthogonal, thereby eliminating correlations among the original features and preventing clustering algorithms from being biased toward certain directions due to redundant features [55]. K-means is an unsupervised classification, which is based on distance between data samples by choosing an appropriate distance formula to measure similarity of data [56]. The larger the distance, the less similarity [57]. The K-means clustering algorithm was selected for its efficiency in handling large sample sizes and its effectiveness in revealing intrinsic grouping structures within multidimensional data [56]. This study introduces the elbow rule for initial judgment to identify the optimal number of clusters. The findings indicate that the quantity of clusters varies between 4 and 9, and the trend of decreasing intra-cluster square error (SSE) flattens out, demonstrating good structural stability. The Silhouette Score and Calinski–Harabasz index are further used as evaluation indices for K-means algorithm clustering. It is found that, when the clustering result is 6 categories, the clustering algorithm demonstrates high effectiveness in identifying distinct regimes (two indices are 0.30 and 3064.58). Relevant model validation metrics are listed in Table A3.

The selection of the K value is based, in part, on the Hierarchical Density-Based Spatial Clustering of Applications with Noise (HDBSCAN) method. The advantage of this method lies in its ability to identify the optimal K without requiring subjective selection. Therefore, the optimal K value is generated directly by this method. If we adopt a method that does not involve human intervention, the optimal cluster K output based on the HDBSCAN results constitutes an objective selection. On the other hand, based on the Silhouette Score and Calinski–Harabasz index, we have also supplemented the performance of other clustering methods in Appendix A.4. For instance, Hierarchical Density-Based Spatial Clustering of Applications with Noise is a density-based hierarchical clustering algorithm capable of automatically determining the number of clusters [58]. This eliminates the need to prespecify the number of clusters or employ other means to evaluate potential cluster counts [59]. However, both the Silhouette Score (0.052) and Calinski–Harabasz (459.22) index for this method were inferior to those obtained using K-means. Another group selected the Gaussian mixture model, a probabilistic clustering algorithm that supports soft clustering and yields more flexible results compared to K-means [60]. However, when applying the Gaussian mixture model for clustering in this study, both metrics remained lower than those achieved by K-means (0.25, 1492.12). Therefore, the clustering method extracted in this study emphasizes the primary morphological characteristics of blocks. For related tables and descriptions, see Appendix A.4.

Based on functional attributes and feature types of various types of CMBs in the real cityscape, six types of CMBs in the block were named. The six types of blocks were named as Semi-open Space (SOS), High-rise Impervious Core (HIC), Function-oriented Blocks (FOB), Blue–Green Space (BGS), Balanced Built–Green Blocks (BB) and Open Space (OS), and characteristics and typical landscapes are shown in Section 4.1.

3.3. Detections of Hotspots and Coldspots

Distribution index (DI) is the ratio of the weight-average molecular weight to the number-average molecular weight. DI was used at a spatial scale to quantify and characterize LST spatial patterns, as well as to identify hotspots and coldspots [61]. This method makes it easy

to identify carrier features that are relatively dominant in hotspots or coldspots. The DI is calculated to identify hotspots (coldspots) within each CMB, according to:

$$DI_{\mathrm{h}} = \frac{S_{\mathrm{h}i}}{S_i} / \frac{S_{\mathrm{h}}}{S} \quad (1)$$

$$DI_c = \frac{S_{ci}}{S_i} / \frac{S_c}{S} \quad (2)$$

where $S_{\mathrm{h}i}$ (S_{ci}) stands for the area of high (cold) temperature areas of the i-th block type, and S_i refers to the total area in i-th block type. S_{h} (S_c) and S are high (cold) temperature area and total area.

DI is a powerful tool that transforms complex multifactorial influences into scientific, flexible, and practical comparable quantitative metrics [62]. This method can be applied to thermal environment management, sustainable design, and policy formulation. On the one hand, as a quantitative indicator, DI is better suited for characterizing and analyzing thermal environmental characteristics at the block scale. On the other hand, as a proxy variable, DI can, to some extent, enhance the comparability of thermal environmental behavior across different seasons. Therefore, this study utilizes DI to quantify the contribution of each CMB type [63]. If DI is larger than 1, this implies that the proportion of the block category is higher, which is the main heat (cold) source [64].

3.4. Analysis of Multifactorial Drivers of LST

3.4.1. Potential LST Driving Factors of Four Hierarchies

A total of 16 contributing factors at four levels of "2D–3D–spectral dimension (spectrum)–urban functional characteristics" were introduced into the XGBoost-SHAP model to explore the LST driving mechanism at the block scale in each season. The calculation methods of the contributing factors and their meanings are shown in Table 1. These variables were chosen to represent the physical and anthropogenic processes influencing the urban surface energy balance. Simultaneously, quantifiability is ensured through RS imagery, spatial data, and POI data. The definitions of each factor and the main references are provided in Table 1. The standard calculation formulas for commonly used spectral indices are presented in Table A2.

Table 1. Four-level factors.

Level	Factors	Meaning	References
Spectral	NDVI	Indicates vegetation growth status	[65]
	EVI	Vegetation indices for urban contexts. EVI measures the greenness or physiological activity of vegetation	[66]
	NDBI	Indicates the distribution of buildings in the city	[67]
	MNDWI	Indicates the distribution of water bodies in an urban context	[65]
Two-dimensional (2D)	VCD	Degree of vegetation cover. VCD measures the degree of vegetation shading or coverage proportion	[26]
	FVC	Block greening levels	[68]
	RD	Length or area of road network	[69]
	ISD	Proportion of artificial surface to area of block	[70]
Three-dimensional (3D)	VMH	Vertical height of vegetation	[26]
	FAR	The proportion of building area to block area	[71]
	MBH	Vertical distance of the buildings	[26]
	SVF	Influence of buildings on sky shading	[72]
Urban functional characteristics	POI	Places of particular significance or function	[73]
	AOI	An information layer, which also encompasses four fundamental attributes. It is primarily used to represent area-based geographic entities on maps	[74]
	FM	Degree of compositing of different functional types in the block	[74]
	MBM	Quantification of the degree of disorder in built environment	[51]

3.4.2. Bayesian-Optimized XGBoost-SHAP Model

Bayesian optimization is used in this study to fine-tune hyperparameters, boosting predictive performance and minimizing computational costs. The primary approach is to iteratively revise the posterior distribution of the objective function using historical hyperparameter results and selecting those with the highest anticipated modification. During each iteration, Bayesian optimization carefully manages the trade-off between exploration and exploitation, directing computational resources toward regions most likely to optimize model performance [47]. The specific model validation parameters are listed in Table A6. Additionally, this study employs five-fold cross-validation. The training data is randomly shuffled and evenly divided into five equal parts (n_splits = 5), each referred to as a fold. By setting random_state = 7, the data partitioning remains consistent across each code execution. Specific RMSE, mean absolute error (MAE), or explainable variance values are provided in Appendix A.2.

XGBoost is an ensemble machine learning algorithm built upon the gradient boosting decision tree, incorporating a second-order Taylor expansion in its objective function [75]. XGBoost, as an efficient gradient boosting algorithm, demonstrates outstanding performance in big data processing [44]. Research indicates that XGBoost excels in studies related to urban layout and LST, owing to its triple advantages of high predictive power, computational efficiency, and portability [45]. This is achieved through the use of a second-order derivative of loss function, within a gradient boosting framework, supplemented by a regularization term [54].

SHAP values, which stem from the Shapley value, were introduced to facilitate the interpretation of machine learning model outputs [46]. They ensure fairness and reasonableness in the attribution process. SHAP is used as a measure to assess the contribution of each characteristic to a predicted consequence for a given sample [76]. Building on the XGBoost regression model outlined earlier, this research used the SHAP method to evaluate the contribution of feature variables to model predictions. SHAP is a model interpretation tool, not a tool for identifying causality. For the specific XGBoost objective function and SHAP model function, see Appendix A.2.

4. Results

4.1. Block-Scale Multidimensional Canopy Morphology Characteristics

This study divides the study area into six types of composite morphological block (CMB) to explore differences in LST distribution among different urban block types (Figure 3, Table 2). The statistics show that BB accounts for the largest proportion of the area (43.46%). BGS represents the smallest proportion (3.53%) and is mainly concentrated in ecological nodes and large-scale urban green space systems, such as the Olympic Forest Park and Temple of Heaven Park. Furthermore, SOS is primarily distributed in the northeastern zone between the Third and Fourth Ring Roads. In contrast, HIC is scattered across areas around the Fourth Ring Road, excluding the southern region. FOB is widely distributed in the Fengtai District and Yizhuang. OS is relatively scattered and is mainly concentrated in parts of the region enclosed by the Second and Fifth Ring Roads, such as the Summer Palace and Yuyuantan Park.

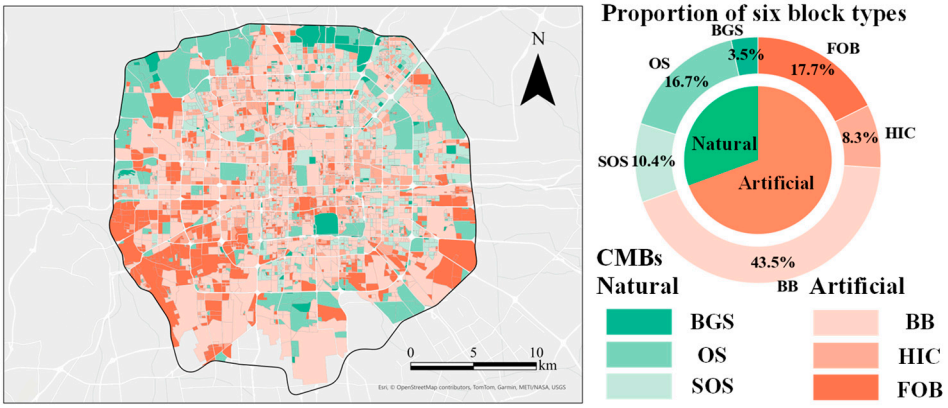


Figure 3. Distribution of Composite Morphological Blocks (CMBs) (Semi-open Space (SOS), High-rise Impervious Core (HIC), Function-oriented Blocks (FOB), Blue–Green Space (BGS), Balanced Built–Green Blocks (BB) and Open Space (OS)).

Table 2. Description of the Composite Morphological Blocks (CMBs).

Block Type	Acronym	Description	Typical Landscape
Blue–Green Space	BGS	Highest average height and density of vegetation	Olsen Park, Temple of Heaven
Open Space	OS	Large green areas in the suburbs	Summer Palace, Yuyuantan Park
Semi-open Space	SOS	Sparse patches, mixed with small parks; highest median average building heights	Beihai Park
Balanced Built–Green Blocks	BB	Large patches, evenly distributed, mixed architectural vegetation	Nanyuan, Forbidden City
High-rise Impervious Core	HIC	High building density; highest mean average building heights	School
Function-orientated Blocks	FOB	Highest impervious surface density	South West Fourth Ring Road area, Coking Plant

To reveal potential associations between spatial attribute differences within CMBs and the urban thermal environment, this study calculated the mean, median, and standard deviation of four CMB metrics (Table 3). In terms of CMB types, BGS exhibits higher vegetation density and higher mean values of vegetation canopy height than OS. Conversely, the mean building height of FOB is lower than that of HIC, while exhibiting a high degree of ISD. Its building form is relatively low, with more pronounced horizontal expansion, owing to constraints related to historical and cultural preservation, industrial layout, and land use functions. Finally, among the two block types with similar building volumes, SOS exhibits higher vegetation canopy height and vegetation density than BB, indicating a higher level of greening.

Table 3. Statistics of values for different CMBs.

Block Type	Average Building Height (m)			Mean Vegetation Height (m)		
	Mean	Median	Std.	Mean	Median	Std.
BGS	9.65	9.89	10.08	5.28	5.02	1.46
OS	6.73	7.31	6.36	2.58	2.51	0.83
SOS	26.16	24.58	6.97	2.87	2.77	0.66
BB	20.56	20.42	4.61	1.64	1.62	0.39
HIC	29.41	27.84	7.35	0.76	0.77	0.42
FOB	12.06	14.21	7.03	0.61	0.62	0.38

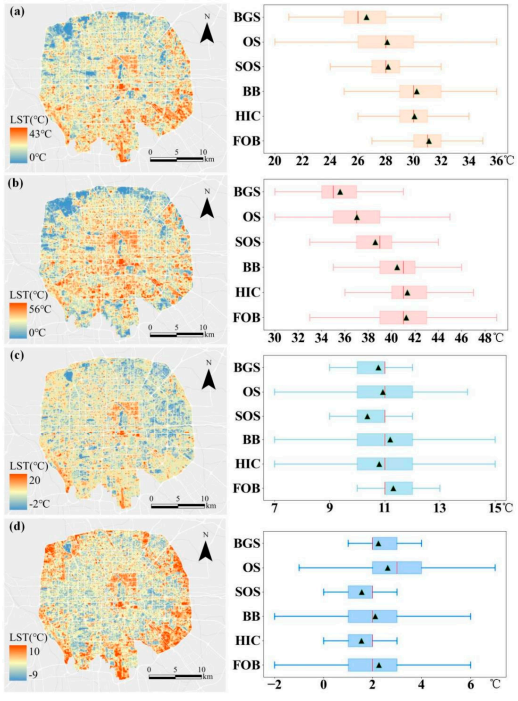
Table 3. *Cont.*

Block Type	Impervious Surface Density (%)			Vegetation Density (%)		
	Mean	Median	Std.	Mean	Median	Std.
BGS	0.22	0.23	0.12	0.77	0.76	0.12
OS	0.52	0.54	0.14	0.44	0.43	0.11
SOS	0.58	0.59	0.08	0.42	0.41	0.08
BB	0.74	0.74	0.05	0.26	0.26	0.05
HIC	0.87	0.86	0.07	0.13	0.14	0.07
FOB	0.89	0.88	0.07	0.11	0.12	0.06

4.2. Spatiotemporal LST Patterns in CMBs

4.2.1. Seasonal LST Variations

CMBs in the central urban areas display notable spatial and temporal variations in their average LSTs across seasons (Figure 4, left). The average LST in spring was 29.66 °C, and the overall distribution showed a decreasing trend from northwest to southeast. The average temperature rose to 39.68 °C in summer, exhibiting a ring-like distribution characterized by lower values around the periphery and higher values in the center. We hypothesize that this pattern may result from building shadows reducing the amount of shortwave solar radiation reaching the ground surface. However, confirming this causal relationship requires further mechanistic analysis combining higher-resolution remote sensing data, radiative transfer models, and field observations. The average LST dropped to 11.03 °C in autumn, exhibiting a nearly north–south symmetrical pattern. The average LST was 2.12 °C in winter, with a ring-like distribution characterized by higher values in the center, lower values in the middle, and a subsequent increase towards the periphery.



Block Types	Spring LST(°C)			Summer LST(°C)			Autumn LST(°C)			Winter LST(°C)		
	Mean	Median	Std	Mean	Median	Std	Mean	Median	Std	Mean	Median	Std
BGS	26.62	26.00	2.42	35.59	35.00	2.83	10.77	11.00	1.17	2.24	2.00	1.17
OS	28.11	28.00	3.50	37.04	37.00	3.20	10.92	11.00	1.59	2.61	3.00	1.49
SOS	28.16	28.00	2.36	38.61	39.00	2.93	10.36	11.00	1.50	1.56	2.00	1.20
BB	30.24	30.00	2.16	40.48	41.00	2.76	11.19	11.00	1.32	2.11	2.00	1.34
HIC	30.06	30.00	2.16	41.34	41.00	2.24	10.80	11.00	1.51	1.54	2.00	1.24
FOB	31.12	31.00	2.41	41.24	41.00	2.88	11.31	11.00	1.65	2.26	2.00	1.43

Figure 4. Spatial distribution of LSTs (**left**; (**a**–**d**) spring, summer, autumn, and winter), box plot of seasonal LSTs in different types of block forms (**right**) and statistical value (**bottom**).

The box plot (Figure 4, right) indicates that LST differences between different building form types are more pronounced in autumn and winter. Areas with taller building forms tend to exhibit relatively lower LST, which may be related to enhanced shading effects and seasonal differences in energy exchange. Each box along the horizontal axis represents the dispersion of LST values within the same category. The vertical axis shows the distribution of LST values across different land cover categories. From a seasonal perspective, the block type with the lowest building height and highest impervious surface density, FOB, exhibited higher LSTs than other CMB types in spring (31.12 ± 2.41 °C), autumn (11.31 ± 1.65 °C), and winter (2.26 ± 1.43 °C). In contrast, BGS, which is dominated by green space and characterized by high canopy height and extensive green space coverage, exhibited lower LSTs in spring (26.62 ± 2.42 °C), summer (35.58± 2.83 °C), and autumn (10.77 ± 1.17 °C). In addition, blocks with high vegetation density, such as SOS, generally exhibited lower LSTs than built-up areas. This further highlights the role of vegetation density in moderating block-scale LST. In contrast, the average LST of SOS was lower than that of BGS in winter. This may be attributed to vegetation dormancy and the freezing of water bodies, which reduce surface heat absorption capacity.

Analysis of variance (ANOVA) F-tests ($p < 0.05$) showed significant differences in LSTs across different CMB types (Figure 4). At the horizontal spatial scale, higher building densities led to higher average LSTs in summer ($LST_{FOB} > LST_{BB} > LST_{SOS}$). The highest LST (56 °C) occurred in FOB during summer, indicating the considerable influence of building density on LST patterns in low-rise CMBs. In the vertical dimension, LST shows an overall downward trend as average building height increases ($LST_{FOB} > LST_{BB} > LST_{HIC}$). This phenomenon may be related to increased shading caused by taller building forms, reduced solar radiation on the ground surface, and changes in local energy exchange conditions.

4.2.2. Varied Responses of LSTs to CMBs

High-level zones were generally located in central regions inside the Second Ring Road. A prominent feature of this region is the presence of extensive impervious surfaces and significant anthropogenic heat emissions. Conversely, low-level zones were mainly located in forest parks such as Beihai Park, where water and vegetation contribute significantly to cooling. The cooling effect is mainly associated with heat absorption and the high albedo of water. Additionally, high-value areas exhibit a broad distribution during spring and autumn, each accounting for over 70% of the total area. Multiple spatial clusters primarily form in southern regions. Most high-level zones are situated between the Second and Fifth Ring Roads. The rank of LSTs at the same locations was opposite in summer and winter, except for localized areas such as Beihai Park.

DI is employed to determine each CMB's contribution to the overall thermal and cooling environment (Figure 5). The distribution of LST categories within the six CMBs is presented in Figure 6. From the analysis of each block category, FOB was mainly composed of high (7.72%, 3.63%, 8.47%, and 3.04% from spring to winter, respectively) and subhigh levels (8.28%, 6.92%, 7.57% and 4.66% from spring to winter). It had hotspot DI values greater than 1 (i.e., 1.85, 1.96, 1.24, and 1.14 from spring to winter) and contributed significantly to LST. In contrast, coldspot DI values were lower than 1 (i.e., 0.03, 0.27, 0.84, and 0.87 from spring to winter). Next, BB had the second-highest hotspot DI value after FOB (1.10, 1.05, 1.09, and 0.95 from spring to winter). Although FOB has the highest hotspot DI value (2.38), its influence was limited owing to its proportion of only 17.70% within the Fifth Ring Road. Although the hotspot DI value of BB was lower than that of FOB, it covers a wide area (43.46%) within the study area, resulting in greater spatial spillover and cumulative thermal effects. The concentration of high-rise buildings and impervious surfaces was primarily observed in HIC. It had the second-highest hotspot DI values after BB (0.91, 1.49, 0.82, and 0.36 from spring to winter). On the other hand,

SOS contains a certain number of buildings, but its green space coverage is relatively high. The coldspot DI values were the highest among the four block types (5.92,3.99 from spring to summer). Both OS and BGS were dominated by water bodies or green spaces. OS had more low-level areas than BGS due to the strong heat absorption and evaporative cooling effects of water. In autumn, the coldspot DI value of OS was higher than that of BGS. In contrast, BGS was dominated by vegetation cover, which is an important LST buffer after water bodies. Building aggregation has the most pronounced impact on hotspot formation in FOB (hotspot $DI_{FOB} > DI_{BB} > DI_{HIC} > DI_{SOS}$). In summary, 2D and 3D canopy morphology significantly influence spatial and temporal temperature variations within CMBs.

	Spring	Summer	Autumn	Winter
Block types		Hot-Spot DI Values		
SOS	0.20	0.21	0.48	0.26
HIC	0.91	**1.49**	0.82	0.36
FOB	**1.85**	**1.96**	**1.24**	**1.14**
BGS	0.11	0.09	0.65	0.84
BB	**1.10**	**1.05**	**1.09**	0.95
OS	0.59	0.30	**1.00**	**1.79**
Minimum				**Maximum**

	Spring	Summer	Autumn	Winter
Block types		Cold-Spot DI Values		
SOS	**1.05**	**1.06**	**1.38**	**1.48**
HIC	0.10	0.07	0.86	**1.47**
FOB	0.03	0.27	0.84	0.87
BGS	**5.92**	**3.99**	0.60	0.76
BB	0.16	0.51	0.40	0.99
OS	**3.60**	**2.84**	**2.64**	0.67
Minimum				**Maximum**

Figure 5. DI values of CMBs (In the figure, red (blue) indicates Hot-Spot DI Values (Cold-Spot DI Values), the darker the color, the higher the value).

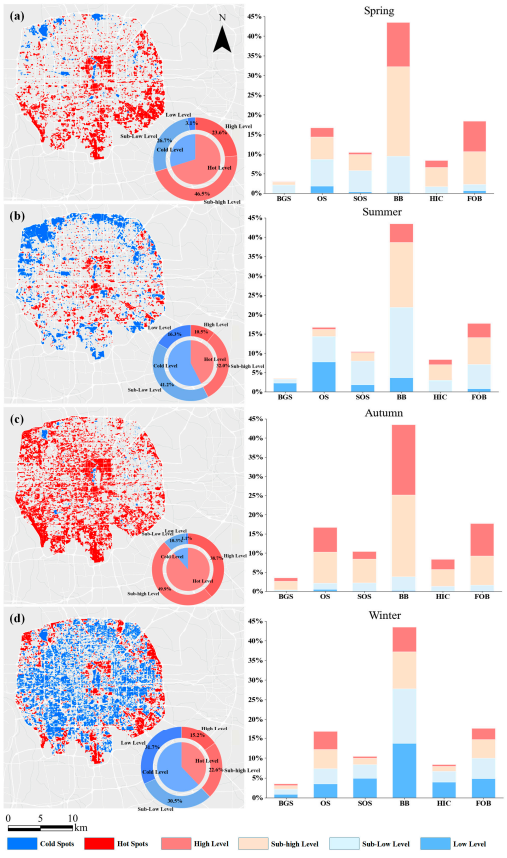


Figure 6. Classified LSTs and area proportion (**left**; (**a**–**d**) represent spring, summer, autumn and winter, respectively) and proportional stacked bar charts representing classified LST levels across different CMBs (**right**).

4.3. Block-Scale LST Driving Forces Across Different Seasons

4.3.1. The Relative Contribution Rank of 16 Factors

Figure 7 presents the relative importance and direction of various metrics influencing LST, reflecting its dynamic variation patterns. This study emphasized that the importance of influencing factors varies across seasons. The MBH index is particularly significant for LST across all seasons of the year. As a result, we conducted a detailed examination of the CMB metrics to rank their importance and contributions. NDBI has a significant impact on urban LST, which is particularly pronounced during spring and summer. Following NDBI, built-related indicators, such as MBH, ISD, and SVF, all exhibit positive impacts, except for MBH in spring. The analysis revealed that urbanized zones exerted a stronger effect on high temperatures through the process of heat absorption and storage. Meanwhile, MBH exhibits a negative influence on LST. This is consistent with the mechanism by which elevation and shaded surfaces influence LST. On the other hand, FVC fully performs its transpiration cooling and shading functions in summer. It plays a key role in alleviating urban high temperatures. MBH and ISD also showed comparable importance scores.

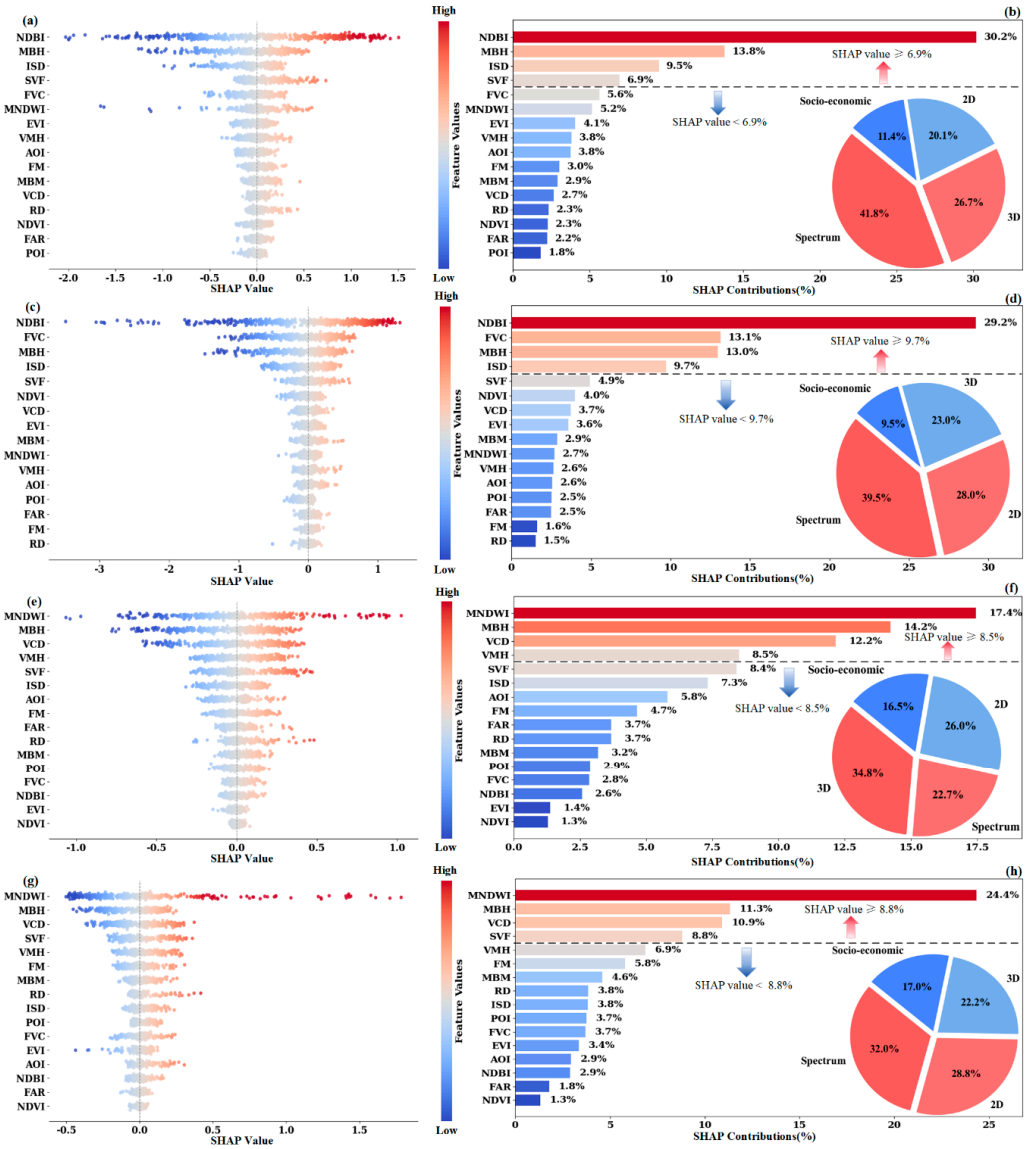


Figure 7. Global interpretation (**left**) and contribution (**right**) of metrics on LST (the two groups from (**a**–**h**) in order of spring, summer, autumn, and winter, respectively. The *X*-axis represents the percentage contribution of SHAP value for that feature. The *Y*-axis represents different factors).

The impact of MNDWI on LST is most pronounced during autumn and winter and exhibits a negative effect on LST (Figure 7). Research indicates that, due to the specific heat capacity of water bodies during the cooling process, their ability to regulate LST is strongest during autumn and winter. This enables LST in water-covered areas to remain consistently low in cold environments. Additionally, MBH, VCD, and VMH exhibit a negative effect on LST, except for VMH in autumn. This demonstrates a clear impact of vegetation and building height on LST in autumn. Accordingly, this result provides support for the selection of block delineation metrics in this study. MBH, VCD, and SVF also impacted LST in winter. This indicates that gaps between buildings enhance the surface's ability to absorb thermal radiation. Although individual feature contributions are generally low, Figure 7 shows that the core feature set used in this study to classify block categories dominates the cumulative SHAP values across SHAP plots for all four seasons. This is despite the model predictions stemming from a nonlinear combination of multiple interacting characteristics. The urban morphological dimensions represented by the classification system exhibit a significant association with surface temperature. This underscores its importance in explaining spatial temperature variations.

4.3.2. The Marginal Effects of Dominant Driving Factors

The feature dependence plots of SHAP were employed to reflect marginal effects (Figures 8 and 9). The impact of the main elements on LST showed nonlinear responses and seasonal differences. This reflects the dynamic complexity of the formation mechanism of the urban thermal environment. The metrics demonstrated relatively stable positive effects, except for MBH in spring. The warming effect diminishes when ISD exceeds approximately 0.8. For SVF, a negative effect was observed until 0.2, followed by a positive effect on increasing SVF. When MBH values were below 20, they showed a slight decrease, while values beyond 20 showed a clear decreasing pattern. In summer, NDBI and ISD exhibited a negative effect on LST. NDBI showed a relatively stable effect on LST, while the effect of ISD became more evident within the range of approximately 0.60 to 0.80. On the contrary, FVC and MBH still showed negative marginal effects. When MBH exceeds 20, its cooling effect is most pronounced. After that, the trend gradually weakens. FVC was similar to NDBI, showing relatively stable changes.

All four indicators in the graph showed negative marginal effects except for VMH in autumn, with VCD, in particular, showing a trend that slowed down. On the contrary, VMH showed a stable positive effect. MNDWI showed a slight positive effect within the range of -0.1 to -0.05. For MBH, the trend slows down when it is less than 20. In winter, MNDWI and VCD were the main cooling factors, both of which showed large negative slopes. VCD had a particularly significant cooling effect on LST at low to moderate values (< 0.4) and leveled off beyond 0.4. On the other hand, MBH showed a three-stage variation, exhibiting a slight increase below 10, a slight decrease within the range of approximately 10 to 25, and a significant decrease beyond approximately 20. In addition, SVF showed a positive marginal effect on LST in winter. When its value exceeds 0.2, the trend shifts from a moderate increase to a significant increase. In summary, the marginal effects of main metrics exhibit a high degree of seasonal heterogeneity and nonlinear characteristics and also present complex threshold effects. The warming effect of NDBI and ISD is greatest in warm seasons. The cooling effect of MNDWI and VCD is significant in cold seasons.

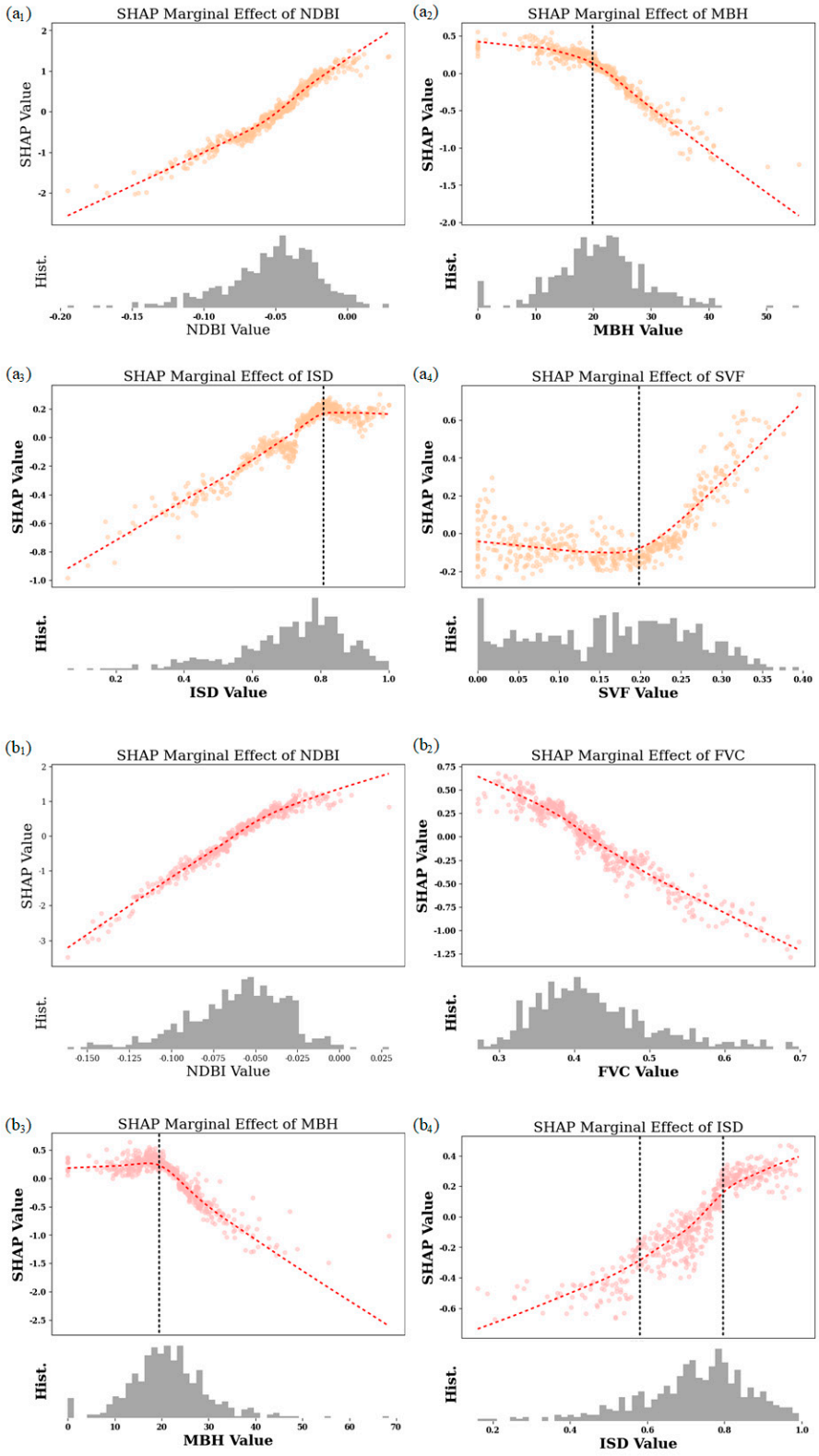


Figure 8. Marginal effects of main driving factors in (**a$_1$**–**a$_4$**) spring and (**b$_1$**–**b$_4$**) summer (The *X*-axis represents the range of feature values for this feature, while the *Y*-axis shows its SHAP value).

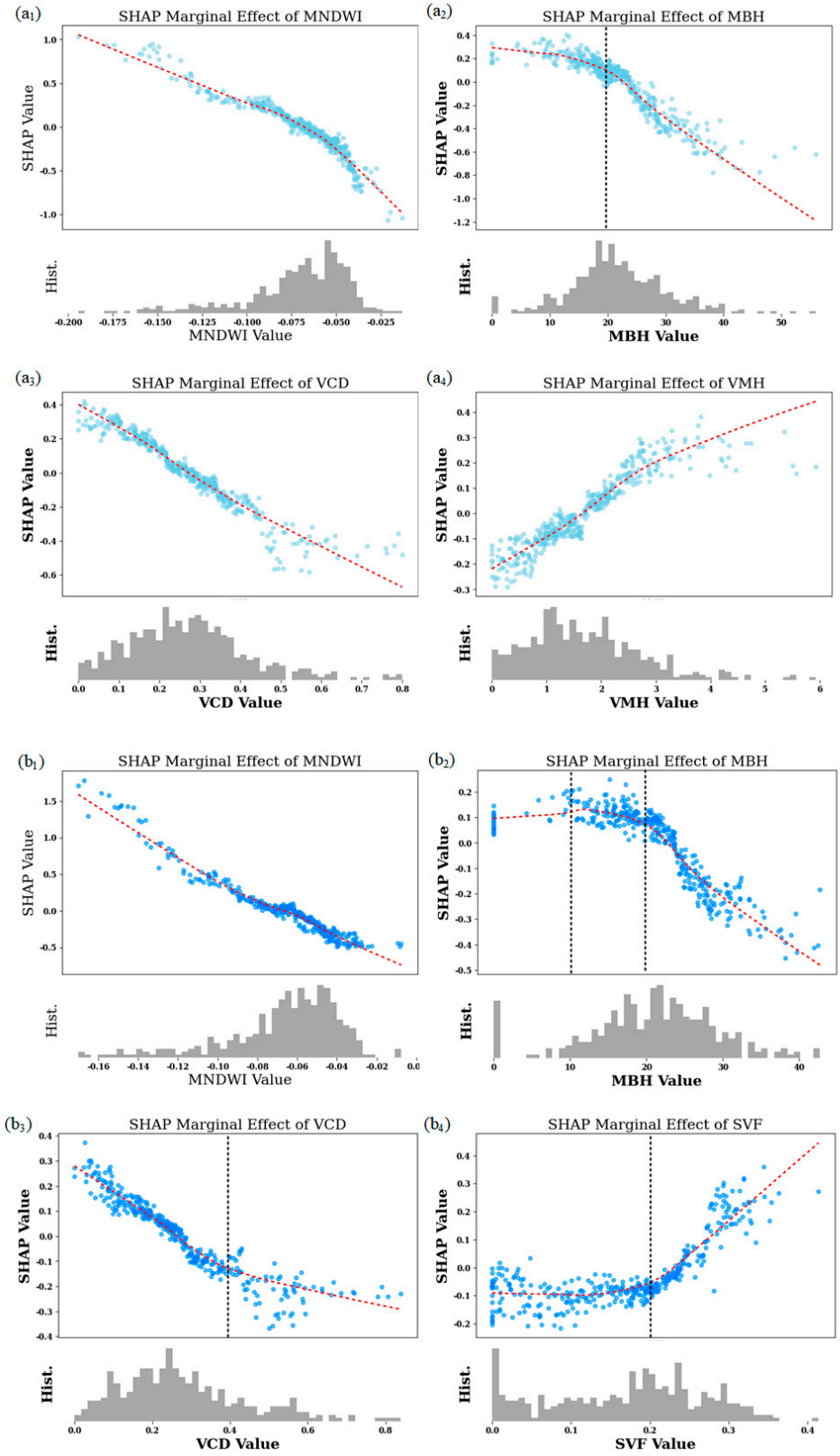


Figure 9. Marginal effects of main driving factors in (**a$_1$**–**a$_4$**) autumn and (**b$_1$**–**b$_4$**) winter (The *X*-axis represents the range of feature values for this feature, while the *Y*-axis shows its SHAP value).

4.3.3. Interaction Effect Analysis

To explore potential associations between LST and control parameters, SHAP interaction plots were generated (Figure 10). This enables a clearer understanding of factors influencing the urban thermal environment. Two sets of factors were selected from the

four dominant factors in each of the four seasons for interaction analysis. One group was ranked first and second, and the other group was ranked second and third. Since the first three dominant factors were consistent in autumn and winter, the SHAP values of MBH and VCD did not differ substantially in winter. At the same time, the secondary dominant factor largely overlaps with the block division factor selected in this study. This indicates that the factors included in this study exert a significant influence on LST.

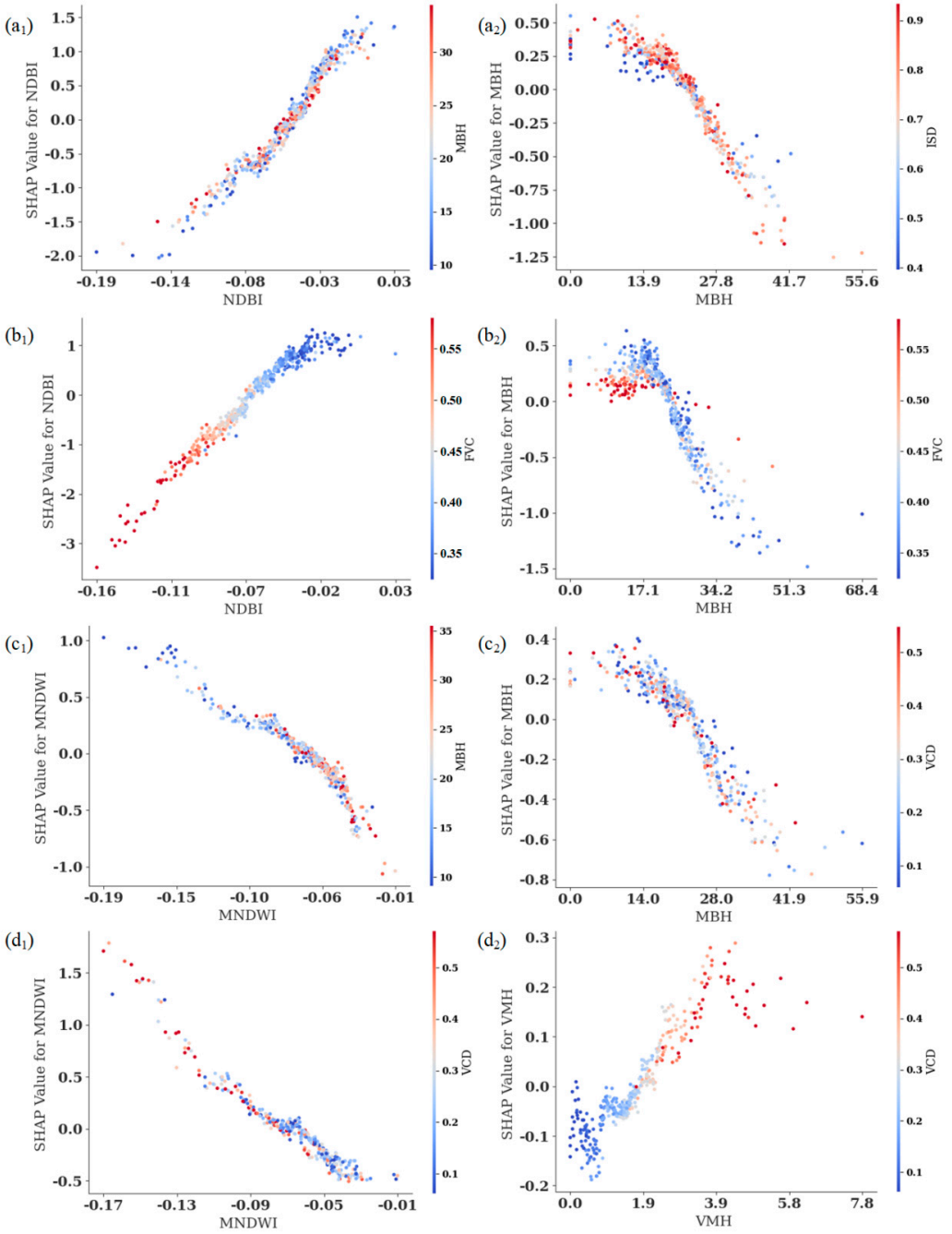


Figure 10. SHAP interaction plot ((**a**$_1$–**a**$_4$) to (**d**$_1$–**d**$_4$) spring, summer, autumn, and winter, respectively, the *X*-axis displays the range of feature values for this feature, the *Y*-axis shows the SHAP value for another feature, indicating the change in model output it would cause).

From the color changes in the correlation matrix, a notable transition occurs between summer NDBI and FVC around NDBI = 0.1. Specifically, when FVC > 0.45 and NDBI < 0.1, NDBI contributes negatively to LST (reducing LST). The opposite condition yields a positive contribution. Regarding MBH and FVC, a higher FVC combined with a lower MBH

contributes less to LST. Lower FVC paired with higher MBH exhibits a negative contribution to LST. In winter, the interaction between VCD and VMH manifests as a shift from a negative to a positive contribution to LST as both values increase. In summer, NDBI and FVC exhibit a distinct transition around NDBI = 0.1. In winter, the interaction between VCD and VMH manifests as a shift from a negative to a positive contribution to LST as both values increase.

Consequently, the clustering factors selected in this study not only possess strong driving forces but also exhibit pronounced interactive effects. These factors demonstrate distinct seasonal variation characteristics. For instance, vegetation cover is a primary determinant, alongside vegetation type, duration of sunshine, and phenological changes [77] and seasonal temperature fluctuations caused by soil moisture content [78]. These factors subsequently influence the distribution of surface energy balance. These contributions reinforce the thermoregulatory mechanisms of multidimensional canopy morphology at the block scale. At the same time, this provides a reference model for sustainable urban development and offers targeted solutions for mitigating heat stress issues.

5. Discussion

5.1. Seasonal Effect of Block-Scale LST Driving Mechanisms

This study further reveals that, when multiple spectral-type factors interact concurrently, their combined explanatory power for LST is marginally lower than that of morphological factor interactions. This phenomenon may stem from the strong correlation between spectral factors and morphological drivers such as building indices and building height [79]. Furthermore, this study supports the notion that clusters of high-rise buildings may suppress vegetation cooling efficiency [80]. Data indicate that, compared with lower-level areas, the cooling effect is reduced by 30% to 50% [81]. This may be related to the relative independence of different regulatory factors in temperature modulation [82].

SHAP analysis reveals significant variations in factor contributions (Figure 11), indicating differing mechanisms and intensities of influence. By comparing prior research on the relationship between 2D and 3D morphological features and LST [49], this study further identifies and validates multiple key drivers affecting LST. These factors include NDBI, MNDWI, ISD, SVF, and MBH [83]. Consistent with existing consensus, MNDWI exhibits a stable marginal negative effect. This confirms its role as a significant factor in the cooling island effect of major cities [84]. Vegetation elements play a central role in reducing LST through shading and evapotranspiration [85]. Moderate greening configurations significantly mitigate heat island intensity [86]. Vegetation height also positively influences cooling capacity [87]. Within the CMB framework of this study, LSTsos and LSTos results further validate the critical role of green spaces in urban thermal regulation.

Conversely, areas with higher development intensity typically exhibit elevated LST, primarily attributed to the presence of dense impervious surfaces [88]. Such materials typically possess low albedo and high thermal capacity, rapidly converting solar radiation into sensible heat [89]. Consistent with this finding, the shading effect associated with increased building height contributes to lower LST [83]. The model shows significant increases in surface heat values for both HIC and FOB areas. This reveals the complexity of the energy balance between building density, ventilation, and shading systems [90]. Spring clustering analysis revealed interactions between key architectural elements (MBH and ISD). High-rise buildings and impervious surface coverage jointly influence surface heat values, suggesting that constrained urban wind corridors and infrastructure expansion may synergistically exacerbate localized heat risks [90]. In contrast, the interaction between building height and vegetation coverage during summer and autumn indicates that integrating tall tree vegetation with building structures can help mitigate heat accumula-

tion [26]. This highlights the potential of high-dimensional greening strategies in urban renewal and microclimate optimization [91].

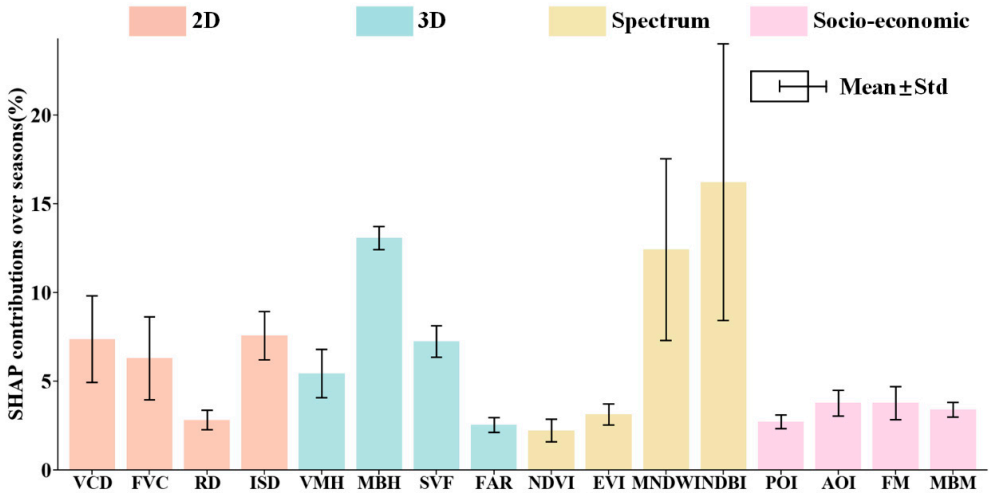


Figure 11. Fluctuations in the SHAP relative contribution of each driving factor across seasons.

Simultaneously, based on the aforementioned interactions, Beijing's urban planning authorities can establish FVC = 0.45 as a critical ecological control threshold for urban planning. Mandatory minimum vegetation coverage requirements should be enforced through local regulations in ecologically sensitive areas, urban wind corridors, and zones surrounding core green spaces [92]. Additionally, stricter upper limits for NDBI should be enforced (e.g., capping NDBI at 0.1). This necessitates low-density, low-intensity development with high-permeability paving and maximized integration of green spaces [93]. In high-temperature zones with NDBI > 0.1, the primary design goal for new green spaces is to achieve an FVC value exceeding 0.45. This necessitates designing multilayered woodlands dominated by trees, rather than single-layer, ecologically less effective lawns or plazas [94]. Small, fragmented, stamp-sized green spaces cannot meet this threshold and offer only limited cooling effects [45]. Regarding MBH and FVC, higher FVC combined with lower MBH contributes less to LST levels. This finding directly supports the thermal environmental superiority of low-rise, low-density development patterns [95].

5.2. Potential Applications of CMB Zoning Scheme

A more refined classification scheme is essential to accurately describe urban form and function [96]. This has led to the emergence of systems such as LCZ, UFZ, and UMB. Compared with existing urban zoning frameworks such as LCZ and UFZ, the CMB proposed in this paper places greater emphasis on the morphological characteristics of the composite canopy formed by buildings and vegetation at the block scale. Specifically, LCZ originates from an urban climatology framework, and its core objective is to identify land cover types with similar local climate responses. Therefore, it is more suitable for fields such as urban heat island monitoring and inter-city comparisons [14]. UFZ, on the other hand, is primarily based on land use and urban functions, emphasizing the spatial differentiation of urban functional types, and is suitable for analyzing the relationship between socioeconomic activities and the thermal environment [18]. Furthermore, existing 2D–3D factors may interact with other environmental variables, such as energy and the carbon cycle [97] and social perception and health [98], which are largely independent of LST. Similarly, urban canopy morphology may also influence other urban environmental factors [5]. For the CMB zoning scheme, the vegetation- and building-related factors used for classification are closely linked to non-LST factors [99]. In alignment with urban ecology

theory, this zoning method can be viewed as an operationalization of urban ecosystem theory [100]. Additionally, this zoning method demonstrates notable superiority and universality. It is easily replicable and comparable across different cities and scales, as it relies on globally accessible vegetation and building data. The fundamental logic is that many drivers or mitigating factors of environmental health issues are intrinsically and mechanistically linked to building form and vegetation cover [101,102].

On the other hand, the K-means clustering method employed in this study offers flexibility, with its core strength lying in the absence of a fixed threshold requirement [56]. Cities at different development levels have their own thresholds [103]. If fixed thresholds are required for research, existing classification methods can achieve this. Additionally, regarding the difference between clustering and classification, the CMB scheme differs from other systems. Compared to classical classification frameworks such as the LCZ, the CMB places greater emphasis on the two- and three-dimensional structural characteristics of the composite canopy of buildings and vegetation within block units under road segmentation. The LCZ is highly versatile in urban thermal environment research and is suitable for describing differences in local climate types [104]. However, in high-density built-up areas, significant variations in vegetation canopy and block morphology may still exist within the same LCZ type [105]. The CMB proposed in this paper serves as a supplementary classification scheme for thermal environment analysis at the block scale, aiming to more precisely characterize the influence of composite canopy structure on the spatial variation of LST. Taking LCZ as an example (Figure A4), CMB is more flexible in scale on the one hand and accommodates diverse city types on the other. For instance, while this study's CMB categorizes neighborhoods into six distinct types, the figure reveals that LCZ divides areas into numerous fragmented, small-scale blocks [106]. LCZs provide a standardized but fixed-class framework [106], whereas CMB offers a more adaptive block-scale alternative. These fragmented zones are designed for global consistency, whereas CMBs aim for locally optimized morphological homogeneity. Consequently, the results achieve a more balanced neighborhood partitioning, whereas LCZ incorporates excessive mixed information.

In addition, we conducted a clustering analysis on a sample of nearly 20,000 blocks across 10 cities in the Beijing–Tianjin–Hebei urban agglomeration. Based on the Rule of Thumb, setting the number of clusters to six appears to be a reasonable choice (Appendix A.8). Although the sum of squared errors continues to decline when the number of clusters exceeds six, the rate of decline slows significantly, indicating that further increasing the number of categories contributes relatively little to improving the distinction between clusters. It should be noted that this study primarily relies on samples from individual cities. If the scope of the study is expanded to include more complex spatial units, such as suburban areas or other cities, the number of clusters K can be further adjusted based on specific data characteristics and research objectives.

5.3. Implications for Urban Planning

In sustainable urban landscape management, economic feasibility is an unavoidable issue [107]. Since most ecological regulation services are difficult to commercialize, assessing their economic benefits presents significant challenges [108]. This has prompted the exploration of governance pathways that balance economic optimization with ecological sustainability [108]. Compared with high-cost strategies such as optimizing building layouts or upgrading materials, adjusting urban spatial form parameters offers a more cost-effective and feasible approach [109]. This study introduces the concept of fuzzy zoning, using CMBs to replace traditional administrative or functional boundaries. This method effectively reduces costs associated with manually delineating boundaries [110]. CMBs demonstrate strong spatial recognition capabilities at a fine scale and hold signifi-

cant potential for thermal environment governance. Therefore, considering the complex structural–functional relationships between CMBs in urban renewal planning can aid in developing efficient thermal environment intervention strategies.

The driving mechanisms of LST vary by scale, geographical location, and seasonal changes [111]. This study reveals LST patterns and multifactor coupling mechanisms at the block scale. It emphasizes that block categories with significant thermal contributions should be prioritized for remediation, with differentiated management strategies developed based on their impact on the overall thermal environment [112]. Based on this study, and in conjunction with the 14th Five-Year Plan for Urban Climate Adaptation Action and Beijing City Master Plan (https://www.gov.cn/xinwen/2021-03/13/content_5592681.htm (accessed on 4 August 2025); https://www.planning.org.cn/law/view_news?id=7564 (accessed on 4 August 2025)), the core built-up area, primarily represented by BB in this research, emphasizes reducing climate risks to critical infrastructure and historic cultural cities. Additionally, regarding contiguous built-up areas, FOB prioritizes synergistically enhancing climate adaptation capacity across urban and rural areas. The objective is to effectively mitigate various climate risks, increase and optimize urban green spaces, and implement shading strategies [113]. Developing and improving the ventilation corridor system in the central urban area can enhance overall air circulation within the built-up zone (Beijing Master Plan). By reducing the ISD from an extremely high level (>0.8) to the 0.6–0.8 range, its warming effect on LST diminishes. In certain seasons, it may even exhibit a cooling effect due to material properties [114]. HIC prioritizes enhancing the climate resilience of socioeconomic systems by advancing functional restructuring and strengthening service support capabilities. Further development of climate-adaptive ecological networks is required (https://sthjj.beijing.gov.cn/bjhrb/index/xxgk69/zfxxgk43/fdzdgknr2/zcfb/2024bzcwj/543352535/index.html (accessed on 4 August 2025)). The plan includes enhancing green landscapes along major highways, waterways, and railways and establishing nine wedge-shaped green ecological corridors. It also requires connecting central urban areas, emerging towns, and cross-regional urban clusters. Research indicates that, when MBH exceeds 20 m, its cooling effect becomes pronounced and sustained. Therefore, through planning guidance, high-rise building clusters should form effective shading networks, particularly in pedestrian walkways and public plazas, to deliver cooling services [115]. OS, BGS, and SOS prioritize ecological conservation, biodiversity enhancement, and the provision of ecological products. When vegetation canopy density reaches approximately 0.4, cooling capacity begins to decrease. Finally, when vegetation canopy height exceeds 3 m, cooling effectiveness diminishes. Integrating blue–green spaces, including river systems, lakes, parks, green areas, and slow-moving transportation networks helps establish a citywide greenway system [9]. Establishing a blue network system comprising water bodies, waterfront green corridors, and waterfront spaces supports this objective [116].

When exploring how to apply these findings to the scenario value of future urban heat disaster prediction and early warning systems, different governance entities should adopt tailored approaches. For urban planners, cooling strategies can be prioritized for implementation in specific zones based on distinct regional classifications. For instance, in block types characterized by high impervious surface density and dispersed building distribution, new development projects should be strictly mandated to meet green space ratios [117], use high-reflectivity materials [118], and incorporate planned ventilation corridors [73]. In mixed-use areas like BB, where buildings and vegetation coexist, regulations and protective planning should safeguard existing cooling islands from erosion by high-density development, ensuring the sustainability of their cooling benefits [73]. By incorporating heat safety as a core metric into the planning decision-making process upfront, new high-risk zones can be avoided at the source. Additionally, for community managers, when heatwave warnings

are issued, they can rapidly identify the highest-risk zones within their jurisdiction based on block typology. This enables prioritizing the placement of temporary cooling centers within or adjacent to high-risk zones [102]. Additionally, the zoning results provide scientific decision-making support and evidence for funding applications for community-level microrenewal projects [119].

5.4. Limitations and Future Prospects

Although this study proposes an innovative neighborhood clustering scheme, the following limitations remain. This clustering method may be primarily applicable to scenarios within the study area. Other cities will require reclustering analyses based on their specific characteristics. It should be noted that the thresholds provided in this paper are based on a sample from Beijing, and their applicability in other cities or regions remains to be further verified. These thresholds are highly dependent on the dataset and may be influenced by factors such as the urban morphological context, the range of variable distributions, sample size, and model structure. Therefore, they have limitations in terms of their applicability as universal urban design rules [120]. This study is a case study, and the applicability of its classification results to other regions or different temporal scales remains to be further verified. Future research could enrich neighborhood clustering factors to ensure that the results more closely align with actual landscape features. Furthermore, the number of clusters, K, can be flexibly set and optimized based on the specific research subjects, regional characteristics, and research objectives. Additionally, the SHAP-value-based analysis aims to interpret the predictive relationships captured by the XGBoost model [121]. Although SHAP has strong explanatory properties, it cannot be used for causal inference. To confirm causal relationships, future studies will need to combine higher-resolution RS data, radiative transfer models, or field observations. To ensure data quality, there are temporal discrepancies among the various data sources. However, these temporal discrepancies between multiple data sources may, to some extent, increase the uncertainty of the results [122]. In future research, we will adopt a data system with synchronized time series to enhance the robustness of seasonal comparisons and mechanism analyses. Meanwhile, seasonal LSTs derived from single-frame remote sensing imagery may still be subject to short-term meteorological fluctuations, such as rainfall, brief cloud cover, or extreme heat events. Future research may further explore more comprehensive high-resolution imagery resources or conduct in-depth analyses of LST effects across different community types under diurnal conditions. Integrating indicators that more accurately reflect human thermal comfort and heat balance, such as mean radiant temperature (MRT), universal thermal climate index (UTCI), or physiologically equivalent temperature (PET), is recommended [123]. This will facilitate a more comprehensive assessment of thermal exposure risks at the pedestrian level. Finally, regarding the remote sensing and morphological data employed, individual trees may lack sufficient spatial detail in imagery for canopy height data, making it challenging to capture complete morphology even at 1 m resolution. Low shrubs occupy only 1–4 pixels per plant, potentially limiting the performance of image-based features. Overall, this research methodology provides a more reliable theoretical foundation for urban planning. Future studies should strengthen empirical exploration across multiple spatiotemporal scales to establish more universal and adaptive pathways for regulating urban thermal environments. This will support the implementation of scientifically grounded urban governance and planning interventions within complex systems.

6. Conclusions

Existing block classification methods lack adequate measures of vegetation canopy characteristics. The nonlinear response of block surface temperatures to urban canopy morphology

across different seasons has not been sufficiently examined. This study comprehensively estimates the correlation between CMBs and LST. The study reveals the complex driving effects of 2D, 3D, spectral, and urban functional factors on seasonal LST variations. Finally, we conclude that: (1) CMBs serve as a component-based framework for analyzing block morphology and, in the case study of this research, demonstrate the potential to identify spatial clustering patterns associated with high and low temperatures. FOB and HIC exhibit higher LST, while BGS and OS demonstrate lower LST. (2) During spring and summer, construction-related factors play a relatively significant role in explaining LST in high-temperature blocks. Whereas in autumn and winter, vegetation and water bodies played a relatively significant role in explaining LST in low-temperature blocks. This pattern suggests that anthropogenic factors account for a larger proportion of the variation in LST during the warmer seasons. As cooler seasons progress, natural factors increasingly influence the thermal environment. (3) Certain driving factors (such as ISD) exhibit a significant marginal warming effect within the area inside Beijing's Fifth Ring Road, with this effect gradually intensifying until it reaches a critical threshold (0.8). MBH shows a linear cooling trend within the area inside Beijing's Fifth Ring Road, accompanied by a persistent buffering effect. There are slight differences in the thresholds of the driving effects of various factors within the area inside Beijing's Fifth Ring Road. (4) Nonlinear interactions between 2D and 3D canopy morphological factors, as well as with other hierarchical factors, are more pronounced than interactions between spectral factors and other dominant factors. This finding also suggests that the proposed CMB scheme may be a feasible approach for characterizing the spatiotemporal patterns of thermal environments. In conclusion, CMBs show potential as a useful tool for evaluating urban environments with diverse spatial formations through a flexible unsupervised clustering approach. Seasonal analysis of the block-scale thermal patterns based on the CMB framework provides a reference for rational urban management.

Author Contributions: Conceptualization, D.H.; methodology, X.L., W.P. and M.X.; software, X.L. and M.X.; validation, X.L. and F.G.; formal analysis, X.L.; investigation, X.L. and W.P.; resources, J.W. and F.G.; data curation, J.W. and F.G.; writing—original draft preparation, X.L.; writing—review and editing, J.W., D.H. and W.P.; visualization, X.L.; supervision, D.H.; project administration, D.H.; funding acquisition, D.H. All authors have read and agreed to the published version of the manuscript.

Funding: This research was funded by the National Natural Science Foundation of China, grant number 42301371, and the Fundamental Research Funds for the Central Universities, grant number 2652024002.

Data Availability Statement: The raw data supporting the conclusions of this article will be made available by the authors on request.

Acknowledgments: The authors would like to thank the anonymous reviewers for their kind suggestions and constructive comments. We acknowledge all WUDAPT contributors for providing the training areas for our city/cities of interest. All authors have read and agreed to the published version of the manuscript.

Conflicts of Interest: The authors declare no conflicts of interest. The funders had no role in the design of the study; in the collection, analyses, or interpretation of data; in the writing of the manuscript; or in the decision to publish the results.

Abbreviations

The following abbreviations are used in this manuscript:

CMB	Composite morphological block
LST	Land surface temperature
BH	Building height
NDBI	Normalized difference built-up index

SDG 11	Sustainable Development Goal 11
UHI	Urban heat island
UCL	Urban canopy layer
RS	Rmote sensing
AT	Air temperature
LCZ	Local climate zone
2D	Two-dimensional
3D	Three-dimensional
RMSE	Root mean square error
OSM	OpenStreetMap
GADM	Global Administrative Areas
GEE	Google Earth Engine
OLI	Operational Land Imager
VCD	Vegetation canopy density
VMH	Vegetation mean height
FAR	Floor area ratio
MBH	Mean building height
SVF	Sky view factor
FM	Functional mix
MBM	Mean building mass
ISD	Impervious surface density
RD	Road density
NDVI	Normalized difference vegetation index
MNDWI	Modified normalized difference water index
EVI	Enhanced vegetation index
FVC	Fractional vegetation cover
SOS	Semi-open Space
HIC	High-rise impervious core
FOB	Function-oriented Blocks
BGS	Blue-Green space
BB	Balanced Built–Green Blocks
OS	Open Space
DI	Distribution index
MAE	Mean absolute error
MRT	Mean radiant temperature
UTCI	Universal thermal climate index
PET	Physiologically equivalent temperature

Appendix A

Appendix A.1 Data Source

Table A1. Datasets utilized in this study.

Data	Composition	Scale	Sources	Time (Day Month Year)	Apply	Related Factors
Vegetation canopy	Gaofen-7 stereo satellite data; On-site measurement data	1 m	https://github.com/Jiahao-WW/3Dvegetation-mt2unetplus (accessed on 4 August 2025)	1 January 2021	Calculation of average vegetation height in blocks	Vegetation canopy density (VCD), vegetation mean height (VMH)

Table A1. *Cont.*

Data	Composition	Scale	Sources	Time (Day Month Year)	Apply	Related Factors
Building data	Google Earth image; POI	1 m	https://doi.org/10.6084/m9.figshare.27992417.v2 (accessed on 4 August 2025)	1 January 2022	Calculation of average building heights in blocks	Floor area ratio (FAR), mean building height (MBH), sky view factor (SVF), functional mix (FM), mean building mass (MBM)
Impervious surface data	Vegetation canopy data; water distribution data	1 m	https://www.openstreetmap.org (accessed on 4 August 2025)	1 January 2021	Impervious surface density calculation	Impervious surface density (ISD)
Block parcel data	Road data; administrative area data	1 m	https://figshare.com/articles/dataset/MSDCW_Dataset_and_Code/26021314 (accessed on 4 August 2025)	1 January 2021	Complex morphological block clustering	Road density (RD)
Land surface temperature	Landsat 8 TIRS	30 m	https://developers.google.com/earth-engine/datasets/catalog/LANDSAT_LC08_C02_T1_L2 (accessed on 4 August 2025)	2 May 2021 6 August 2021 26 November 2021 10 January 2022	Spatial and temporal variations of thermal conditions within blocks	LST
Spectral image	Landsat 8 OLI	30 m	https://developers.google.com/earth-engine/datasets/catalog/LANDSAT_LC08_C02_T1_L2 (accessed on 4 August 2025)	2 May 2021 6 August 2021 26 November 2021 10 January 2022	Calculation of spectral factors	Normalized difference vegetation index (NDVI), normalized difference built-up index (NDBI), modified normalized difference water index (MNDWI), enhanced vegetation index (EVI), fractional vegetation cover (FVC)
AOI; POI	OSM map	1 m	https://www.openstreetmap.org (accessed on 4 August 2025)	1 January 2021	Calculation of urban functional factors	AOI, POI

Table A2. Four-level factors formula.

Level	Factors	Computing Equation
Spectral	NDVI	$NDVI = \frac{NIR+Red}{NIR-Red}$
	EVI	$EVI = 2.5 \times \frac{NIR-Red}{NIR+6\times Red-7.5\times Blue+1}$
	NDBI	$NDBI = \frac{SWIR-NIR}{SWIR+NIR}$
	MNDWI	$MNDWI = \frac{Green-SWIR}{Green+SWIR}$
Two-dimensional (2D)	VCD	$D = \frac{S_{Vegetation}}{S_{total}}$
	FVC	$FVC = \frac{NDVI-NDVI_{min}}{NDVI_{max}-NDVI_{min}}$
	RD	$D = \frac{L}{S}$ L is total length of road; S is standard block area
	ISD	$D = \frac{\sqrt{A}}{1+\sqrt{Var(X)+Var(Y)}}$ where A denotes impervious surface area and Var(X) and Var(Y) represent variances in the X-coordinate and Y-coordinate directions, respectively

Table A2. *Cont.*

Level	Factors	Computing Equation
Three-dimensional (3D)	VMH	$\frac{1}{n}\sum_{i=1}^{n} h_i$
	FAR	$P = \frac{A}{S}$ A and S are the total building and site area respectively
	MBH	$\frac{1}{n}\sum_{i=1}^{n} h_i$
	SVF	$1 - \frac{A_{OBST}}{A_{TOTAL}}$ A_{OBST} is the area of sky obscured by obstacles A_{TOTAL} is the total area of the hemispherical sky
Urban functional characteristics	POI	$POI = \frac{A}{S}$ A: Number of points in the region S: Area of the region
	AOI	$D = 1 - \sum_{i=1}^{n} P_i^2$ P_i: Proportion of area occupied by the i: Land use type in block n: Number of land use types
	FM	$H = -\sum_{i=1}^{n} Q * \ln(Q_i)$ Q_i: Proportion of i-th land use type in the block n: Total number of land use types
	MBM	$T_{yk} = \sum_{m=1}^{M} \left(\frac{\sum_{n=1}^{N_{yn}} S_{yknm}}{N_m} \right)$ $Q_{iy} = \sum_{k=1}^{6} \frac{T_{yk}}{M}$ M: Total count of buildings within the buffer zone surrounding each building centroid N_{yn}: Total count in viewpoint m in year y k: Type of building disorder S_{yknm}: Score (0 or 1, indicating presence or absence) of the n-th streetscape image in viewpoint m for disorder type k in year y T_{yk}: Total disorder score for all streetscape viewpoints m in buffer zone of building i for disorder type k in year y

Appendix A.2 Model Validation Metrics

XGBoost incorporates both the loss function and a regularization term in its objective function (Equations (A1) and (A2)), where loss function quantifies deviation between predicted and observed values. The regularization term serves to constrain the model's complexity, thereby preventing overfitting.

$$\text{objective} = \sum_{i=1}^{n} (y_i, \hat{y}_i) + \Omega \sum_{k=1}^{K} (f_k) \tag{A1}$$

$$\Omega(f_k) = \gamma T + \frac{1}{2}\lambda \parallel \omega \parallel^2 \tag{A2}$$

n indicates quantity of training data; y_i is actual LST of i-th block, while $\hat{y}_i$ is predicted LST for that block; $l(y_i, \hat{y}_i)$ quantifies discrepancy between observed and predicted values. f_t refers to predictive function of t-th base learner; T refers to child node count; ω indicates average value of the dependent variable in training set for each child node; γ regulates the child node count; $\Omega(f_k)$ represents regularization term that limits complexity of model; λ serves as a regularization parameter to ensure average of target arguments in child nodes does not grow too large. In this study, a block refers to the minimum analytical unit defined by the CMB classification.

SHAP constructs an additive explanatory model where all features are treated as contributors. For each prediction sample, the model generates a predicted value, and the SHAP value represents the numerical contribution assigned to each feature in that sample.

$$\varphi_i = \sum_{S \epsilon F \setminus \{i\}} \frac{|S|!(|F| - |S| - 1)!}{|F|!} \left[f_{S \cup \{i\}} \left(x_{S \cup \{i\}} \right) - f_S(x_S) \right] \tag{A3}$$

i is a specific feature, F represents a complete set of characteristics, S is a subset of characteristics excluding characteristics i, x_S corresponds to input values for features in S, $f_{S \cup \{i\}}$ is a model built using characteristics i, $|S|!$ represents factorial of number of characteristics in S, f_S is a model without it. If φ_i is positive, the feature is regarded as a positive factor; otherwise, it is considered a negative factor.

Explained variance is a fundamental statistical concept, with its core purpose being to measure a model's ability to account for data variation or its predictive accuracy. In regression analysis, explained variance can be used to assess how well a model's predicted values align with actual observed values [124].

$$\text{explained variance score} = 1 - \frac{\text{Var}(\text{y} - \hat{\text{y}})}{\text{Var}(\text{y})} \tag{A4}$$

where: y is the actual target variable (i.e., the true value), $\hat{\text{y}}$ is the model's predicted output value; $\text{Var}(\text{y} - \hat{\text{y}})$ represents the residual sum of squares divided by the sample size (i.e., the square of the standard deviation of the error term), $\text{Var}(\text{y} - \hat{\text{y}})$ and Var (y) are the variance of the target variable y.

The closer the explained variance score is to 1, the stronger the model's ability to explain variations in the datasets and the better its predictive performance. The closer it is to 0, the weaker the model's ability to explain data variations.

Mean absolute error (MAE) is the average of the absolute values of the errors, calculated using the following formula.

$$MAE = \frac{\sum_{i=1}^{n} |y_i - \hat{y}_i|}{\text{n}} \tag{A5}$$

Here, n represents the number of samples; y_i denotes the true value; and $\hat{\text{y}}_i$ is the predicted value.

MAE is insensitive to outliers but fails to reflect the distribution of prediction errors.

Root mean square error (RMSE) is the square root of MSE, calculated as

$$RMSE = \sqrt{\frac{\sum_{i=1}^{n} \left(y_i - \widehat{y}_i \right)^2}{n}} \tag{A6}$$

Here, n denotes the number of samples; y_i represents the true value; and $\hat{\text{y}}_i$ denotes the predicted value.

RMSE is sensitive to outliers, but it effectively reflects the distribution of prediction errors.

The RMSE, MAE, or SHAP variance values obtained by running the model are shown in Table A3.

Table A3. Model validation metrics.

Season	RMSE	MAE	SHAP Variance Values	SHAP Ranking Stability
Spring	1.13	0.86	0.554	0.999
Summer	1.13	0.89	0.6977	0.996
Autumn	0.95	0.63	0.3462	0.997
Winter	0.63	0.50	0.5017	0.997

To assess the reliability of feature contributions, we applied a bootstrap resampling approach (n = 30) to the XGBoost–SHAP model. For each resample, SHAP values were recalculated, and the mean ± 95% confidence intervals were derived for major predictors. The results confirmed that the relative feature importance remained consistent across resamples, indicating stable nonlinear responses.

Appendix A.3 Autocorrelation Between Potential Driving Factors

To explore the synergistic and antagonistic relationships among various drivers and investigate the autocorrelation among 16 potential drivers, we plotted correlation heatmaps for four seasons (Figure A1). Results indicate that NDVI, EVI, FVC, and VCD exhibit high positive correlations (r > 0.85) across all four seasons. Furthermore, NDBI exhibits significant negative correlations with both NDVI and EVI across all seasons, indicating that areas with high building density typically feature lower vegetation coverage. NDBI shows a significant positive correlation with ISD, suggesting that more urbanized areas possess higher imperviousness, particularly pronounced during summer. The correlation between VMH and VCD remained consistently high (>0.9), indicating a stable positive relationship between vegetation height and canopy density. Concurrently, ISD showed significant negative correlations with both VCD and VMH during summer and autumn, suggesting that the expansion of impervious surfaces may weaken vegetation growth structures, thereby impairing surface temperature regulation capabilities. Regarding building parameters, MBH positively correlates with ISD during summer, as high-rise-dense areas typically feature greater impervious coverage. FAR maintains consistent positive correlations with urbanization indicators like NDBI and ISD, particularly pronounced in winter and spring.

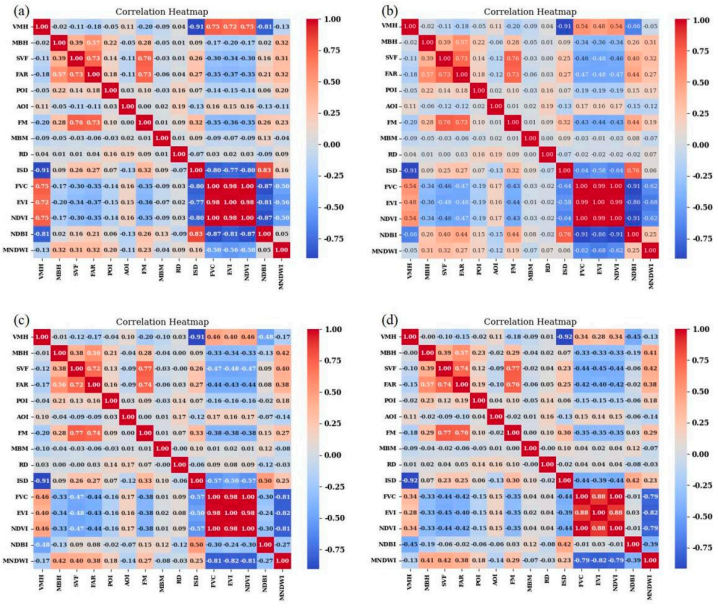


Figure A1. Heatmap ((**a**–**d**) spring, summer, autumn, and winter).

Appendix A.4 Other Metrics or Methods

Table A4. Clustering Evaluation Results for Different K Values.

K	Silhouette Score	Calinski–Harabasz
4	0.27	2316.83
5	0.30	2335.92
6	0.31	2271.61
7	0.30	2200.81
8	0.30	2140.71
9	0.29	2051.10

Hierarchical Density-Based Spatial Clustering of Applications with Noise (HDBSCAN):

The advantage of this method lies in its ability to identify the optimal K without requiring subjective selection. The optimal K it identified was the six categories used in this study. However, both the Silhouette Score (0.052) and Calinski–Harabasz index (459.22) for this method were inferior to those obtained using K-means. Therefore, K-means was ultimately employed.

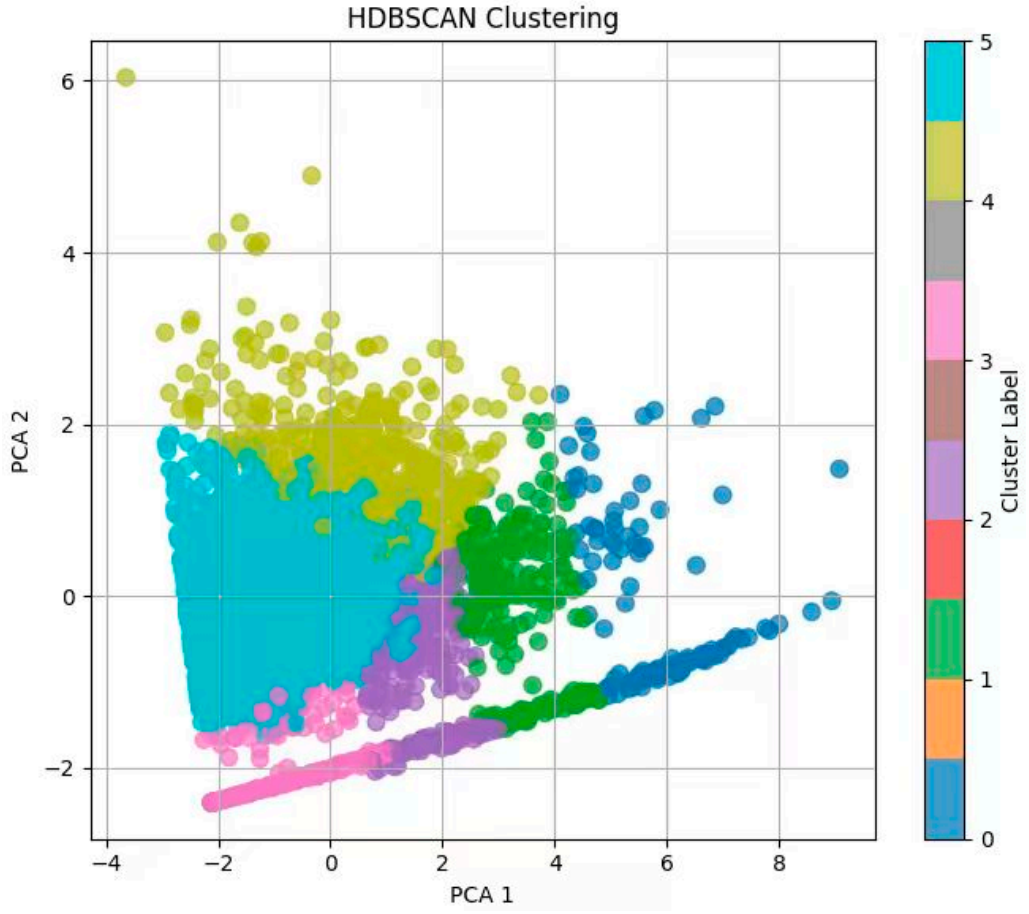


Figure A2. HDBSCAN Clustering.

Gaussian mixture model (GMM):

When performing clustering with a Gaussian mixture model, both metrics remain lower than those of K-means even when K = 6 (0.25, 1492.12).

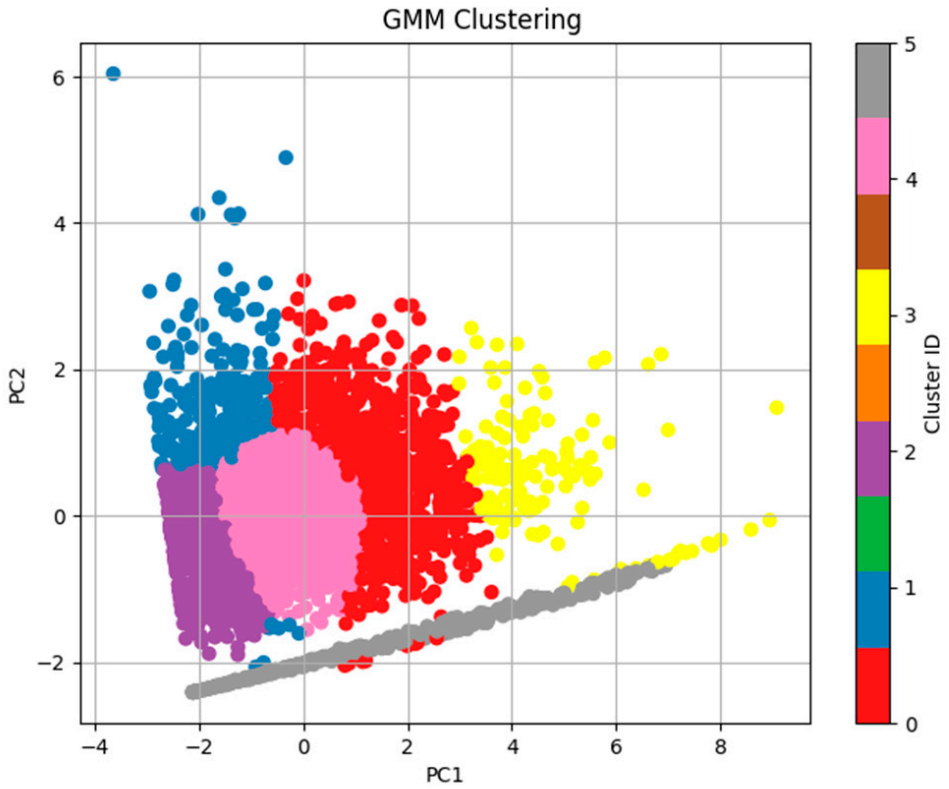


Figure A3. GMM Clustering.

Table A5. Model Comparison.

Method	Principle	Silhouette Score	Calinski–Harabasz Index	Advantages
HDBSCAN	HDBSCAN is a hierarchical extension of DBSCAN, combining the principles of density-based clustering and hierarchical clustering. Its core lies in representing the clustering structure of data through a density hierarchy tree.	0.05	459.22	1. HDBSCAN is a density-based hierarchical clustering algorithm capable of automatically determining the number of clusters without requiring prior specification of cluster size or reliance on alternative methods to assess potential cluster counts. 2. The HDBSCAN algorithm is capable of handling datasets with significant variations in density distribution. 3. Provides an automated cluster extraction mechanism, eliminating the need for manual parameter adjustment or observation of the reachability map. 4. With fewer parameter dependencies, HDBSCAN requires only one primary parameter: MinClusterSize.

Table A5. *Cont.*

Method	Principle	Silhouette Score	Calinski–Harabasz Index	Advantages
GMM	GMM posits that data is generated by a mixture of Gaussian distributions (normal distributions), with each Gaussian distribution corresponding to a cluster. Unlike K-means, GMM is a probabilistic model where the probability of each point belonging to each cluster can be calculated, rather than being rigidly assigned to a single cluster.	0.25	1492.12	1. Supports soft clustering (outputting probabilities), yielding more flexible results. 2. Capable of capturing complex nonspherical distributions, offering broader applicability. 3. Model parameters may be selected objectively using metrics such as AIC/BIC.

Appendix A.5 Model Validation Parameters

This study employs five-fold cross-validation. The training data is randomly shuffled and evenly divided into five equal parts (n_splits = 5), each referred to as a fold. By setting random_state = 7, the data partitioning remains consistent across each code execution.

Table A6. Model Validation Parameters.

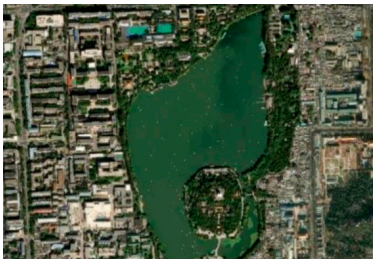
Parameter	Description	Effect	Typical Value Range
max_depth	Maximum depth of a tree	Control the complexity of the model; deeper trees can capture more feature interactions but are prone to overfitting.	[3, 10]
n_estimators	Number of trees in the integration	Determines the model's learning ability and training time; excessive amounts may lead to overfitting.	[50, 1000]
learning_rate	Learning rate/ shrinkage factor	Control the contribution of each tree to the final prediction. Smaller values require more trees but may yield better generalization.	[0.01, 0.3]
subsample	Subsampling ratio of training instances	Randomly select a portion of the data to train each tree, preventing overfitting.	[0.5, 1.0]
reg_alpha	L1 regularization term	Control model complexity to aid feature selection.	[0, 1]
min_child_weight	Minimum instance weight required for child nodes	Control tree splitting; larger values make the model more conservative.	[1, 20]
colsample_bynode	Feature sampling ratio during node splitting	Increase randomness to prevent overfitting.	[0.5, 1.0]

Appendix A.6 CMB Category

Table A7. CMB Category.

CMB	Core Features	Aerial Imagery
BB	The distribution of buildings and vegetation is relatively uniform. Among the three artificial categories, this type has the lowest impervious surface density and the highest vegetation density and height, while building height is moderate.	

Table A7. *Cont.*

CMB	Core Features	Aerial Imagery
BGS	Vegetation features are clearly visible. Among the three natural types, building height is moderate, vegetation height and density are the highest, and impervious surface density is the lowest.	
FOB	This category is characterized by significant human activity and a high degree of impervious surfaces. Among the three artificial categories, impervious surface density is the highest, while building height, vegetation density, and vegetation height are the lowest.	
HIC	Buildings in this category are tall and densely concentrated. Among the three artificial categories, impervious surface density, vegetation density, and vegetation height are intermediate, while building height is the highest.	
OS	Green space is widely distributed. Among the three natural types, building and vegetation height are the lowest, while vegetation and impervious surface density are intermediate.	
SOS	Mixed-use green spaces within high-rise buildings. Among the three natural types, building height and impervious surface density are the highest and vegetation height is intermediate; vegetation density is the lowest.	

Appendix A.7 Local Climate Zones (LCZs)

The component morphological block (CMB) framework was designed to complement rather than replace existing urban zoning systems such as the local climate zone (LCZ) scheme. While LCZs provide a globally standardized and physically interpretable classification for climate studies, their fixed land-cover typology may not flexibly adapt to local urban contexts.

It should be noted that the spatial resolutions of the two systems differ, and as CMBs have a finer pixel resolution, the comparison presented here is conceptual rather than pixel-by-pixel, aiming to evaluate classification logic and LST response characteristics. Taking an LCZ as an example [106], we analyze the differences between it and a CMB.

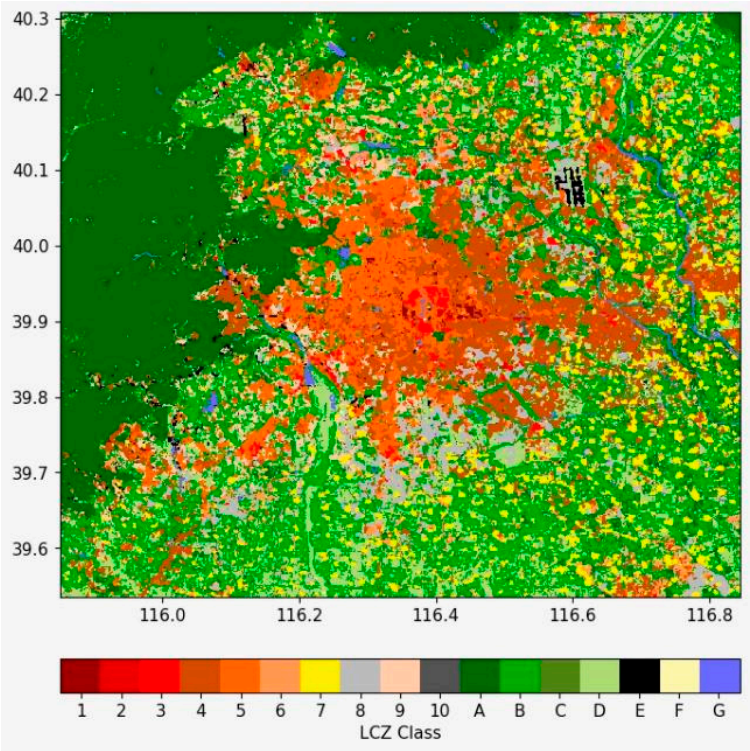


Figure A4. Category Diagram (See Figure A5 for the meaning of the codes).



Figure A5. Explanation of the letters 1–G.

Table A8. Training Information Table.

LCZ Class	Count	Avg. Area (km^2)	Total Area (km^2)	Perimeter (km)	Shape	Vertices
1	15	0.35	5.21	2.57	1.79	8.87
2	6	0.28	1.67	2.54	1.85	10.67
3	13	0.53	6.88	3.09	1.59	9.00
4	35	0.96	33.69	4.28	1.81	10.00
5	21	1.06	22.28	4.35	1.61	9.90
6	22	0.53	11.73	3.08	1.50	7.64
7	23	0.47	10.87	2.99	1.57	9.91
8	10	0.74	7.42	3.65	1.62	9.10
9	5	0.64	3.18	3.53	1.62	10.80
10	5	0.43	2.16	2.60	1.47	6.00
11	18	1.10	19.79	3.23	1.71	13.39
12	14	0.48	6.66	2.66	1.55	7.86
13	11	0.23	2.54	2.11	1.86	11.55
14	28	0.27	7.68	2.25	1.66	8.71
15	19	0.28	5.26	3.01	4.04	12.74
16	6	0.09	0.56	1.31	1.60	9.83
17	21	0.21	4.31	1.81	1.52	6.33

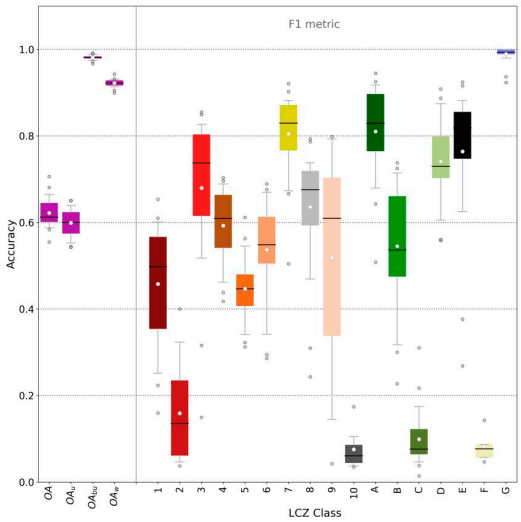


Figure A6. Accuracy Chart (See Figure A5 for the meaning of the codes).

Appendix A.8 Results of the Elbow Rule

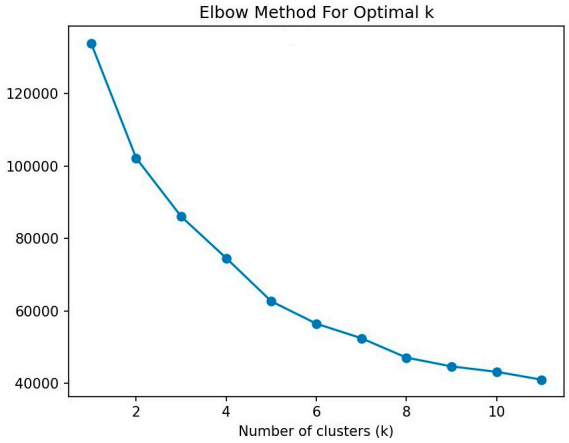


Figure A7. Results of the Elbow Rule for Urban Areas in the Beijing–Tianjin–Hebei Metropolitan Area.

References

1. Deepthi, S.; Sudalaimani, K.; Radhakrishnan, S. Evaluating urban heat island to achieve sustainable development goals: A case study of Tiruchirappalli city, India. *Sustain. Cities Soc.* **2024**, *116*, 105865. [CrossRef]
2. Guo, X.; Du, H.; Zhan, W.; Ji, Y.; Wang, C.; Wang, C.; Ge, S.; Wang, S.; Li, J.; Jiang, S.; et al. Global patterns and determinants of year-to-year variations in surface urban heat islands. *ISPRS J. Photogramm. Remote Sens.* **2025**, *223*, 399–412. [CrossRef]
3. Bao, Y.; Li, Y.; Gu, J.; Shen, C.; Zhang, Y.; Deng, X.; Han, L.; Ran, J. Urban heat island impacts on mental health in middle-aged and older adults. *Environ. Int.* **2025**, *199*, 109470. [CrossRef]
4. Oke, T.R.; Mills, G.; Christen, A.; Voogt, J.A. *Urban Climates*; Cambridge University Press: Cambridge, UK, 2017.
5. Wang, M.; Wang, X.; Luan, Q.; Xu, X. A new perspective to assess urban heat islands by incorporating both canopy and boundary layer air temperature from the view of satellite remote sensing. *Sustain. Cities Soc.* **2025**, *125*, 106315. [CrossRef]
6. Gao, Y.; Zhan, W.; Du, H.; Wang, C.; Wang, S.; Ji, Y.; Ge, S.; Wang, C.; Li, J. Comprehensive assessments of a diagnostic equation for estimating diurnally maximum canopy urban heat island intensity. *Build. Environ.* **2025**, *271*, 112618. [CrossRef]
7. Liang, C.; Serge, A.; Zhang, X.; Wang, H.; Wang, W. Assessment of street forest characteristics in four African cities using google street view measurement: Potentials and implications. *Environ. Res.* **2023**, *221*, 115261. [CrossRef] [PubMed]
8. Lai, J.; Zhan, W.; Quan, J.; Bechtel, B.; Wang, K.; Zhou, J.; Huang, F.; Chakraborty, T.; Liu, Z.; Lee, X. Statistical estimation of next-day nighttime surface urban heat islands. *ISPRS J. Photogramm. Remote Sens.* **2021**, *176*, 182–195. [CrossRef]
9. Xu, Z.; Rui, J. The mitigating effect of green Space's spatial and temporal patterns on the urban heat island in the context of urban densification: A case study of Xi'an. *Sustain. Cities Soc.* **2024**, *117*, 105974. [CrossRef]
10. Mix, C.; Hunt, N.; Stuart, W.; Hossain, A.A.; Bishop, B.W. A Spatial Analysis of Urban Tree Canopy Using High-Resolution Land Cover Data for Chattanooga, Tennessee. *Appl. Sci.* **2024**, *14*, 4861. [CrossRef]
11. Guo, F.; Sun, J.; Hu, D. Surface energy balance-based surface urban heat island decomposition at high resolution. *Remote Sens. Environ.* **2024**, *315*, 114447. [CrossRef]
12. Yang, L.; Yang, X.; Zhang, H.; Ma, J.; Zhu, H.; Huang, X. Urban morphological regionalization based on 3D building blocks—A case in the central area of Chengdu, China. *Comput. Environ. Urban Syst.* **2022**, *94*, 101800. [CrossRef]
13. Zhang, Z.; Luan, W.; Yang, J.; Guo, A.; Su, M.; Tian, C. The influences of 2D/3D urban morphology on land surface temperature at the block scale in Chinese megacities. *Urban Clim.* **2023**, *49*, 101553. [CrossRef]
14. Wang, J.; Yang, J.; Xiao, X.; Bai, Y.; Zou, Q.; He, B. Assessing summer thermal environment in humid cities: Local climate zone perspective. *iScience* **2025**, *28*, 112758. [CrossRef] [PubMed]
15. Wang, B.; Gao, M.; Li, Y.; Li, Z.; Liu, Z.; Zhang, X.; Wen, Y. Unraveling the effects of extreme heat conditions on urban heat environment: Insights from local climate zones and integrated temperature data. *Sustain. Cities Soc.* **2025**, *122*, 106254. [CrossRef]
16. Deng, H.; Feng, J.; Liu, K.; Xiong, Y.; Cao, J. Local climate zone framework: Seasonal dynamics of surface urban heat island and its influencing factors in three Chinese urban agglomerations. *GIScience Remote Sens.* **2025**, *62*, 2490317. [CrossRef]
17. Jing, Y.; Sun, R.; Chen, L. A Method for Identifying Urban Functional Zones Based on Landscape Types and Human Activities. *Sustainability* **2022**, *14*, 4130. [CrossRef]
18. Qi, J.; Xiong, W.; Li, J.; Zheng, J.; Ye, Q.; Hu, M. Investigating non-linear and synergistic effects of urban functional zone morphology on land surface temperature. *Sustain. Cities Soc.* **2025**, *130*, 106546. [CrossRef]
19. Cheng, H.; Cai, Y.; Zhang, D.; Luo, S.; Li, M.; Hu, Y.; Ma, S. Neighboring matters: Quantifying internal morphology and external spatial interactions on land surface temperature among urban functional zones. *Sustain. Cities Soc.* **2025**, *131*, 106689. [CrossRef]
20. Wu, J.; Liu, C.; Wang, H. Analysis of Spatio-temporal patterns and related factors of thermal comfort in subtropical coastal cities based on local climate zones. *Build. Environ.* **2022**, *207*, 108568. [CrossRef]
21. Luo, P.; Yu, B.; Li, P.; Liang, P.; Zhang, Q.; Yang, L. Understanding the relationship between 2D/3D variables and land surface temperature in plain and mountainous cities: Relative importance and interaction effects. *Build. Environ.* **2023**, *245*, 110959. [CrossRef]
22. Wang, Z.; Zhou, R.; Yu, Y. The impact of urban morphology on land surface temperature under seasonal and diurnal variations: Marginal and interaction effects. *Build. Environ.* **2025**, *272*, 112673. [CrossRef]
23. Rizwan, A.M.; Dennis, L.Y.; Chunho, L. A review on the generation, determination and mitigation of Urban Heat Island. *J. Environ. Sci.* **2008**, *20*, 120–128. [CrossRef] [PubMed]
24. Liu, Y.; Huang, X.; Yang, Q.; Jing, W.; Yang, J. Effects of landscape on thermal livability at the community scale based on fine-grained geographic information: A case study of Shenzhen. *Sci. Total. Environ.* **2023**, *905*, 167091. [CrossRef]
25. Wang, K.; Du, J.; Li, C.; Li, M.; Chen, C.; Wang, Z.; Chen, J. Uncovering the coupling mechanisms among urban form, surface thermal environments and air pollution. *Sustain. Cities Soc.* **2025**, *130*, 106537. [CrossRef]
26. Lin, L.; Zhao, Y.; Zhao, J.; Wang, D. Comprehensively assessing seasonal variations in the impact of urban greenspace morphology on urban heat island effects: A multidimensional analysis. *Sustain. Cities Soc.* **2025**, *118*, 106014. [CrossRef]
27. Jia, J.; Jing, Z.; Wang, L.; Yao, Y.; Zhai, Y.; Li, R.; Chang, B.; Lee, S.; Brown, R.D.; Ren, Z. Unraveling the 3D structure of urban green spaces: Key drivers of cooling effects across urban heat scenarios. *Environ. Impact Assess. Rev.* **2026**, *120*, 108409. [CrossRef]

28. Ma, W.; Yu, Z.; Chen, J.; Yang, W.; Zhang, Y.; Hu, Y.; Shao, M.; Hu, J.; Zhang, Y.; Zhang, H.; et al. What drives the cooling dynamics of urban vegetation via evapotranspiration and shading under extreme heat? *Sustain. Cities Soc.* **2025**, *130*, 106659. [CrossRef]
29. Wang, X.; Rahman, M.A.; Mokroš, M.; Rötzer, T.; Pattnaik, N.; Pang, Y.; Zhang, Y.; Da, L.; Song, K. The influence of vertical canopy structure on the cooling and humidifying urban microclimate during hot summer days. *Landsc. Urban Plan.* **2023**, *238*, 104841. [CrossRef]
30. Mun, D.; Kang, G.; Yang, M.; Kim, J. How trees' drag and cooling effects influence airflow and temperature distributions around a street canyon. *Build. Environ.* **2024**, *264*, 111913. [CrossRef]
31. Li, H.; Zhao, Y.; Wang, C.; Ürge-Vorsatz, D.; Carmeliet, J.; Bardhan, R. Cooling efficacy of trees across cities is determined by background climate, urban morphology, and tree trait. *Commun. Earth Environ.* **2024**, *5*, 1–14. [CrossRef]
32. Peng, M.; Huang, H. The Synergistic Effect of Urban Canyon Geometries and Greenery on Outdoor Thermal Comfort in Humid Subtropical Climates. *Front. Environ. Sci.* **2022**, *10*, 851810. [CrossRef]
33. Chen, Y.; Ma, W.; Shao, Y.; Wang, N.; Yu, Z.; Li, H.; Hu, Q. The impacts and thresholds detection of 2D/3D urban morphology on the heat island effects at the functional zone in megacity during heatwave event. *Sustain. Cities Soc.* **2024**, *118*, 106002. [CrossRef]
34. Wang, A.; Dai, Y.; Zhang, M.; Chen, E. Exploring the cooling intensity of green cover on urban heat island: A case study of nine main urban districts in Chongqing. *Sustain. Cities Soc.* **2025**, *124*, 106299. [CrossRef]
35. Chen, J.; Jin, S.; Du, P. Roles of horizontal and vertical tree canopy structure in mitigating daytime and nighttime urban heat island effects. *Int. J. Appl. Earth Obs. Geoinf.* **2020**, *89*, 102060. [CrossRef]
36. Liu, J.; Zhang, S.; Yin, L.; Li, B.; Zhang, B. Exploring the relationship between seasonal variations of land surface temperature and urban morphological factors in complex urban areas. *Environ. Sci. Pollut. Res.* **2023**, *30*, 59861–59876. [CrossRef] [PubMed]
37. Yao, X.; Zeng, X.; Zhu, Z.; Lan, Y.; Shen, Y.; Liu, Q.; Yang, F. Exploring the diurnal variations of the driving factors affecting block-based LST in a "Furnace city" using ECOSTRESS thermal imaging. *Sustain. Cities Soc.* **2023**, *98*, 104841. [CrossRef]
38. Wang, L.; Hou, H.; Weng, J. Ordinary least squares modelling of urban heat island intensity based on landscape composition and configuration: A comparative study among three megacities along the Yangtze River. *Sustain. Cities Soc.* **2020**, *62*, 102381. [CrossRef]
39. Zhang, Q.; Wu, Z.; Yu, H.; Zhu, X.; Shen, Z. Variable Urbanization Warming Effects across Metropolitans of China and Relevant Driving Factors. *Remote Sens.* **2020**, *12*, 1500. [CrossRef]
40. Li, L.; Zha, Y.; Zhang, J. Spatially non-stationary effect of underlying driving factors on surface urban heat islands in global major cities. *Int. J. Appl. Earth Obs. Geoinf.* **2020**, *90*, 102131. [CrossRef]
41. Wu, Z.; Yao, L.; Ren, Y. Characterizing the spatial heterogeneity and controlling factors of land surface temperature clusters: A case study in Beijing. *Build. Environ.* **2020**, *169*, 106598. [CrossRef]
42. Zang, Y.; Huang, G.; Liu, W.; Chen, L.; Wu, D.; Wang, C.; Li, J. Deepurbanmodeller (DUM): A Process-informed neural architecture for high-precision urban surface temperature prediction. *ISPRS Int. Arch. Photogramm. Remote Sens. Spat. Inf. Sci.* **2023**, *XLVIII-1/W*, 71–76. [CrossRef]
43. Wan, Y.; Du, H.; Yuan, L.; Xu, X.; Tang, H.; Zhang, J. Exploring the influence of block environmental characteristics on land surface temperature and its spatial heterogeneity for a high-density city. *Sustain. Cities Soc.* **2025**, *118*, 105973. [CrossRef]
44. Chen, Y.; Yang, J.; Yu, W.; Ren, J.; Xiao, X.; Xia, J.C. Relationship between urban spatial form and seasonal land surface temperature under different grid scales. *Sustain. Cities Soc.* **2023**, *89*, 104374. [CrossRef]
45. He, J.; Shi, Y.; Xu, L.; Lu, Z.; Feng, M.; Tang, J.; Guo, X. Exploring the scale effect of urban thermal environment through XGBoost model. *Sustain. Cities Soc.* **2024**, *114*, 105763. [CrossRef]
46. Li, H.; Yang, J.; Xin, J.; Yu, W.; Ren, J.; Yu, H.; Xiao, X.; Xia, J. Investigating the effect of urban form on land surface temperature at block and grid scales based on XGBoost-SHAP. *Environ. Model. Softw.* **2026**, *195*, 106738. [CrossRef]
47. Cheng, J.; Yang, D.; Qie, K.; Wang, J. Analysis of land surface temperature drivers in Beijing's central urban area across multiple spatial scales: An explainable ensemble learning approach. *Energy Build.* **2025**, *338*, 115704. [CrossRef]
48. Shin, H. XGBoost Regression of the Most Significant Photoplethysmogram Features for Assessing Vascular Aging. *IEEE J. Biomed. Health Inform.* **2022**, *26*, 3354–3361. [CrossRef] [PubMed]
49. Ma, X.; Yang, J.; Zhang, R.; Yu, W.; Ren, J.; Xiao, X.; Xia, J. XGBoost-Based Analysis of the Relationship Between Urban 2-D/3-D Morphology and Seasonal Gradient Land Surface Temperature. *IEEE J. Sel. Top. Appl. Earth Obs. Remote Sens.* **2024**, *17*, 4109–4124. [CrossRef]
50. Wu, J.; Meng, Q.; Gao, L.; Zhang, L.; Zhao, M.; Su, C. A deep learning framework for 3D vegetation extraction in complex urban environments. *Int. J. Appl. Earth Obs. Geoinf.* **2024**, *129*, 103798. [CrossRef]
51. Zhang, Y.; Zhao, H.; Long, Y. CMAB: A Multi-Attribute Building Dataset of China. *Sci. Data* **2025**, *12*, 1–18. [CrossRef]
52. Tang, J.; Xu, L.; Yu, H.; Jiang, H.; He, D.; Li, T.; Xiao, W.; Zheng, X.; Liu, K.; Li, Y.; et al. A dataset of multi-level street-block divisions of 985 cities worldwide. *Sci. Data* **2025**, *12*, 1–15. [CrossRef]
53. Liu, Z.; Lai, J.; Zhan, W.; Bechtel, B.; Voogt, J.; Quan, J.; Hu, L.; Fu, P.; Huang, F.; Li, L.; et al. Urban Heat Islands Significantly Reduced by COVID-19 Lockdown. *Geophys. Res. Lett.* **2022**, *49*, e2021GL096842. [CrossRef]

54. Wang, Y.-Q.; Li, J.-Y.; Liu, B.; Wang, F. [Spatial Heterogeneity of Carbon Emissions from Construction Projects Based on XGBoost-SHAP]. *Environ. Sci.* **2024**, *46*, 4090–4100. [CrossRef]
55. Gao, Y.; Lin, T.; Zhang, Y.; Luo, S.; Nie, F. Robust principal component analysis based on discriminant information. *IEEE Trans. Knowl. Data Eng.* **2021**, *35*, 1991–2003.
56. Gupta, M.K.; Chandra, P. An Empirical Evaluation of K-Means Clustering Algorithm Using Different Distance/Similarity Metrics. In *Proceedings of ICETIT 2019: Emerging Trends in Information Technology, New Delhi, India, 21–22 June 2019*; Springer: Berlin/Heidelberg, Germany, 2019; pp. 884–892.
57. Ye, J.; Yao, X.; Shi, X.; Yang, F. Global vs. local heat patches: Toward a more comprehensive perspective on managing urban overheating—A Shanghai case study. *Sustain. Cities Soc.* **2025**, *129*, 106503. [CrossRef]
58. Li, B.; Liu, K.; Wang, M.; Wang, Y.; Zhuang, L.; Zhu, W.; Li, C.; Zhang, L.; Chen, Y. Evaluating the performance of pixel-based and object-based multidimensional clustering algorithms for automated surface water mapping. *Geo-Spat. Inf. Sci.* **2025**, 1–21. [CrossRef]
59. Stewart, G.; Al-Khassaweneh, M. An Implementation of the HDBSCAN* Clustering Algorithm. *Appl. Sci.* **2022**, *12*, 2405. [CrossRef]
60. Najar, F.; Bourouis, S.; Bouguila, N.; Belghith, S. A Comparison Between Different Gaussian-Based Mixture Models. In *Proceedings of the 2017 IEEE/ACS 14th International Conference on Computer Systems and Applications (AICCSA), Hammamet, Tunisia, 30 October–3 November 2017*; IEEE: New York, NY, USA, 2017; pp. 704–708.
61. Liu, J.; Tian, Y.; Yang, Y.; Zhang, T.; Deng, Y.; Chen, W.; Yin, L.; Zhang, B. Constructing an urban cooling network based on multidimensional influencing factors of urban heat island and local climate zones. *Build. Environ.* **2025**, *289*, 114090. [CrossRef]
62. Huang, X.; Wang, Y. Investigating the effects of 3D urban morphology on the surface urban heat island effect in urban functional zones by using high-resolution remote sensing data: A case study of Wuhan, Central China. *ISPRS J. Photogramm. Remote Sens.* **2019**, *152*, 119–131. [CrossRef]
63. Mottet, A.; Ladet, S.; Coqué, N.; Gibon, A. Agricultural land-use change and its drivers in mountain landscapes: A case study in the Pyrenees. *Agric. Ecosyst. Environ.* **2006**, *114*, 296–310. [CrossRef]
64. Li, W.; Cao, Q.; Lang, K.; Wu, J. Linking potential heat source and sink to urban heat island: Heterogeneous effects of landscape pattern on land surface temperature. *Sci. Total. Environ.* **2017**, *586*, 457–465. [CrossRef]
65. Hu, D.; Meng, Q.; Zhang, L.; Zhang, Y. Spatial quantitative analysis of the potential driving factors of land surface temperature in different "Centers" of polycentric cities: A case study in Tianjin, China. *Sci. Total. Environ.* **2020**, *706*, 135244. [CrossRef]
66. Jiang, Z.; Huete, A.R.; Didan, K.; Miura, T. Development of a two-band enhanced vegetation index without a blue band. *Remote Sens. Environ.* **2008**, *112*, 3833–3845. [CrossRef]
67. Zha, Y.; Gao, J.; Ni, S. Use of normalized difference built-up index in automatically mapping urban areas from TM imagery. *Int. J. Remote Sens.* **2010**, *24*, 583–594. [CrossRef]
68. Carson, T.N.; Ripley, D.A. On the Relation between NDVI, Fractional Vegetation Cover, and Leaf Area Index. *Remote Sens. Environ.* **1997**, *62*, 241–252. [CrossRef]
69. Weng, Q.; Liu, H.; Liang, B.; Lu, D. The Spatial Variations of Urban Land Surface Temperatures: Pertinent Factors, Zoning Effect, and Seasonal Variability. *IEEE J. Sel. Top. Appl. Earth Obs. Remote Sens.* **2008**, *1*, 154–166. [CrossRef]
70. Arnold, C.L., Jr.; Gibbons, C.J. Impervious Surface Coverage: The Emergence of a Key Environmental Indicator. *J. Am. Plan. Assoc.* **1996**, *62*, 243–258. [CrossRef]
71. Sun, Y.; Gao, C.; Li, J.; Wang, R.; Liu, J. Quantifying the Effects of Urban Form on Land Surface Temperature in Subtropical High-Density Urban Areas Using Machine Learning. *Remote Sens.* **2019**, *11*, 959. [CrossRef]
72. Zakšek, K.; Oštir, K.; Kokalj, Ž. Sky-View Factor as a Relief Visualization Technique. *Remote Sens.* **2011**, *3*, 398–415. [CrossRef]
73. Tang, G.; Du, X.; Wang, S. Impact mechanisms of 2D and 3D spatial morphologies on urban thermal environment in high-density urban blocks: A case study of Beijing's Core Area. *Sustain. Cities Soc.* **2025**, *123*, 106285. [CrossRef]
74. Wang, L.; Li, R.; Jia, J.; Zhai, Y.; Tian, Y.; Xu, D.; Chen, Y.; Zhang, X.; Ren, Z.; Ye, Z.; et al. Integrating morphology and vitality to quantify seasonal contributions of urban functional zones to thermal environment. *Sustain. Cities Soc.* **2025**, *120*, 106136. [CrossRef]
75. Kavzoglu, T.; Teke, A. Predictive Performances of Ensemble Machine Learning Algorithms in Landslide Susceptibility Mapping Using Random Forest, Extreme Gradient Boosting (XGBoost) and Natural Gradient Boosting (NGBoost). *Arab. J. Sci. Eng.* **2022**, *47*, 7367–7385. [CrossRef]
76. Deb, D.; Smith, R.M. Application of Random Forest and SHAP Tree Explainer in Exploring Spatial (In)Justice to Aid Urban Planning. *ISPRS Int. J. Geo-Inf.* **2021**, *10*, 629. [CrossRef]
77. Ionita, M.; Vaideanu, P.; Nichita, D.; Nagavciuc, V. Breaking records under clear skies: The impact of sunshine duration and atmospheric dynamics on the 2024 Eastern European extreme summer temperatures. *npj Nat. Hazards* **2025**, *2*, 82. [CrossRef]
78. Tian, R.; Li, J.; Zheng, J.; Liu, L.; Han, W.; Liu, Y. Changes in vegetation phenology and its response to different layers of soil moisture in the dry zone of Central Asia, 1982–2022. *J. Hydrol.* **2025**, *646*, 132314. [CrossRef]

79. Xiang, Y.; Tang, Y.; Wang, Z.; Peng, C.; Huang, C.; Dian, Y.; Teng, M.; Zhou, Z. Seasonal Variations of the Relationship between Spectral Indexes and Land Surface Temperature Based on Local Climate Zones: A Study in Three Yangtze River Megacities. *Remote Sens.* **2023**, *15*, 870. [CrossRef]
80. Chen, Z.; Ye, J.; Liu, Y.; Hu, T.; Dong, J. Global assessment in the effect of urban built-up environment on cooling efficiency of green spaces. *Commun. Earth Environ.* **2025**, *6*, 968. [CrossRef]
81. Chen, W.; Zhang, J.; Shi, X.; Liu, S. Impacts of Building Features on the Cooling Effect of Vegetation in Community-Based MicroClimate: Recognition, Measurement and Simulation from a Case Study of Beijing. *Int. J. Environ. Res. Public Health* **2020**, *17*, 8915. [CrossRef]
82. Pandey, A.; Mondal, A.; Guha, S. Assess the relationship of land surface temperature with nine land surface indices in a northeast Indian city using summer and winter Landsat 8 data. *Cogent Eng.* **2024**, *11*, 2382885. [CrossRef]
83. Hu, D.; Meng, Q.; Schlink, U.; Hertel, D.; Liu, W.; Zhao, M.; Guo, F. How do urban morphological blocks shape spatial patterns of land surface temperature over different seasons? A multifactorial driving analysis of Beijing, China. *Int. J. Appl. Earth Obs. Geoinf.* **2022**, *106*, 102648. [CrossRef]
84. Pritipadmaja; Garg, R.D.; Sharma, A.K. Assessing the Cooling Effect of Blue-Green Spaces: Implications for Urban Heat Island Mitigation. *Water* **2023**, *15*, 2983. [CrossRef]
85. Wang, J.; Zhou, W.; Jiao, M.; Zheng, Z.; Ren, T.; Zhang, Q. Significant effects of ecological context on urban trees' cooling efficiency. *ISPRS J. Photogramm. Remote Sens.* **2020**, *159*, 78–89. [CrossRef]
86. Zhao, J.; Guo, F.; Zhang, H.; Dong, J. Mechanisms of non-stationary influence of urban form on the diurnal thermal environment based on machine learning and MGWR analysis. *Sustain. Cities Soc.* **2024**, *101*, 105194. [CrossRef]
87. He, T.; Hu, Y.; Guo, A.; Chen, Y.; Yang, J.; Li, M.; Zhang, M. Quantifying the impact of urban trees on land surface temperature in global cities. *ISPRS J. Photogramm. Remote Sens.* **2024**, *210*, 69–79. [CrossRef]
88. Guo, A.; Yang, J.; Sun, W.; Xiao, X.; Cecilia, J.X.; Jin, C.; Li, X. Impact of urban morphology and landscape characteristics on spatiotemporal heterogeneity of land surface temperature. *Sustain. Cities Soc.* **2020**, *63*, 102443. [CrossRef]
89. Chen, X.; Wang, Z.; Bao, Y.; Luo, Q.; Wei, W. Combined impacts of buildings and urban remnant mountains on thermal environment in multi-mountainous city. *Sustain. Cities Soc.* **2022**, *87*, 104247. [CrossRef]
90. Xu, H.; Li, C.; Hu, Y.; Li, S.; Kong, R.; Zhang, Z. Quantifying the effects of 2D/3D urban landscape patterns on land surface temperature: A perspective from cities of different sizes. *Build. Environ.* **2023**, *233*, 110085. [CrossRef]
91. Sun, F.; Zhang, J.; Takeda, S.; Cui, J.; Yang, R. Vertical Plant Configuration: Its Impact on Microclimate and Thermal Comfort in Urban Small Green Spaces. *Land* **2024**, *13*, 1715. [CrossRef]
92. Soydan, O. Effects of landscape composition and patterns on land surface temperature: Urban heat island case study for Nigde, Turkey. *Urban Clim.* **2020**, *34*, 100688. [CrossRef]
93. Banerjee, S.; Yik, S.K.; Dzyuban, Y.; Crank, P.J.; Yi, R.P.X.; Chow, W.T. Analysing impacts of urban morphological variables and density on outdoor microclimate for tropical cities: A review and a framework proposal for future research directions. *Build. Environ.* **2022**, *225*, 109646. [CrossRef]
94. Lin, Z.; Xu, H.; Han, L.; Zhang, H.; Peng, J.; Yao, X. Day and night: Impact of 2D/3D urban features on land surface temperature and their spatiotemporal non-stationary relationships in urban building spaces. *Sustain. Cities Soc.* **2024**, *108*, 105507. [CrossRef]
95. Wang, R.; Murayama, Y.; Liu, F.; Zhang, X.; Hou, H.; Morimoto, T.; Derdouri, A. Impact of urban morphology on land surface temperature: A case study of the central Tokyo, Japan. *City Environ. Interact.* **2025**, *28*, 100227. [CrossRef]
96. González, J.E.; Ramamurthy, P.; Bornstein, R.D.; Chen, F.; Bou-Zeid, E.R.; Ghandehari, M.; Luvall, J.; Mitra, C.; Niyogi, D. Urban climate and resiliency: A synthesis report of state of the art and future research directions. *Urban Clim.* **2021**, *38*, 100858. [CrossRef]
97. Du, S.; Zhang, Y.; Sun, W.; Liu, B. Quantifying heterogeneous impacts of 2D/3D built environment on carbon emissions across urban functional zones: A case study in Beijing, China. *Energy Build.* **2024**, *319*, 114513. [CrossRef]
98. Ding, X.; Feng, B.; Wu, J. The influence of two and three-dimensional spatial characteristics of industrial parks on the emotional well-being of employees: A case study of Shenzhen. *Appl. Geogr.* **2024**, *171*, 103367. [CrossRef]
99. Zheng, Z.; Zhao, C.; Yang, G.; Zhou, W.; Wei, B.; Xie, Y.; Peng, Y.; Chen, L.; Yang, Y. Partial offset of soil greenhouse gases emissions by enhanced vegetation carbon uptake upon thermokarst formation. *Natl. Sci. Rev.* **2025**, *12*, nwaf340. [CrossRef]
100. Jaung, W.; Carrasco, L.R.; Richards, D.R.; Shaikh, S.F.E.A.; Tan, P.Y. The role of urban nature experiences in sustainable consumption: A transboundary urban ecosystem service. *Environ. Dev. Sustain.* **2022**, *25*, 601–621. [CrossRef]
101. Xiong, S.; Yang, F.; Gu, C. Exploring spatiotemporal coupling effects between built environment and ecosystem health: Toward static–dynamic sustainable management in waterfront cities. *J. Clean. Prod.* **2025**, *503*, 145389. [CrossRef]
102. Xing, J.; Hu, Z.; Xia, F.; Xu, J.; Zou, E. *Urban Forests: Environmental Health Values and Risks*; National Bureau of Economic Research: Cambridge, MA, USA, 2025.
103. Zhang, H.; Wang, Z.; Chai, J. Land use\cover change and influencing factors inside the urban development boundary of different level cities: A case study in Hubei Province, China. *Heliyon* **2022**, *8*, e10408. [CrossRef]

104. Yang, J.; Yu, W.; Baklanov, A.; He, B.; Ge, Q. Mainstreaming the local climate zone framework for climate-resilient cities. *Nat. Commun.* **2025**, *16*, 1–5. [CrossRef]
105. Joshi, K.; Khan, A.; Anand, P.; Santamouris, M. Linking inter- and intra-LCZ morphological characteristics with outdoor thermal stress and building cooling demand during heatwave conditions. *Energy Build.* **2026**, *352*, 116773. [CrossRef]
106. Demuzere, M.; Kittner, J.; Bechtel, B. LCZ Generator: A Web Application to Create Local Climate Zone Maps. *Front. Environ. Sci.* **2021**, *9*, 637455. [CrossRef]
107. Fu, B.; Liu, Y.; Zhao, W.; Wu, J. The emerging "pattern-process-service-sustainability" paradigm in landscape ecology. *Landsc. Ecol.* **2025**, *40*, 54. [CrossRef]
108. Chen, H. How to assess realized ecosystem services: Indicators, challenges in determining actual use, and suggestions. *Ecosyst. Serv.* **2025**, *76*, 101796. [CrossRef]
109. Ye, Y.; Li, D.; Liu, X. How block density and typology affect urban vitality: An exploratory analysis in Shenzhen, China. *Urban Geogr.* **2018**, *39*, 631–652. [CrossRef]
110. Guo, H.; Dong, L.; Wu, L.; Liu, Y. Tackling spatial heterogeneity in geographical analysis: An overview. *Acta Geogr. Sin.* **2025**, *80*, 567–585.
111. Deng, X.; Yu, W.; Shi, J.; Huang, Y.; Li, D.; He, X.; Xie, Z. Characteristics of surface urban heat islands in global cities of different scales: Trends and drivers. *Sustain. Cities Soc.* **2024**, *107*, 105483. [CrossRef]
112. Qiao, Z.; Lu, Y.; He, T.; Wu, F.; Xu, X.; Liu, L.; Wang, F.; Sun, Z.; Han, D. Spatial expansion paths of urban heat islands in Chinese cities: Analysis from a dynamic topological perspective for the improvement of climate resilience. *Resour. Conserv. Recycl.* **2023**, *188*, 106680. [CrossRef]
113. Feng, R.; Wang, F.; Liu, S.; Qi, W.; Zhao, Y.; Wang, Y. How urban ecological land affects resident heat exposure: Evidence from the mega-urban agglomeration in China. *Landsc. Urban Plan.* **2023**, *231*, 104643. [CrossRef]
114. Lian, D.; Yuan, B.; Li, X.; Shi, Z.; Ma, Q.; Hu, T.; Miao, S.; Huang, J.; Dong, G.; Liu, Y. The contrasting trend of global urbanization-induced impacts on day and night land surface temperature from a time-series perspective. *Sustain. Cities Soc.* **2024**, *109*, 105521. [CrossRef]
115. Kim, J.; Yeom, S.; Hong, T. Analyzing the cooling effect, thermal comfort, and energy consumption of integrated arrangement of high-rise buildings and green spaces on urban heat island. *Sustain. Cities Soc.* **2025**, *119*, 106105. [CrossRef]
116. Zhao, H.; Hu, M.; Zhu, J.; Huang, T.; Zhang, Y.; Li, Y.; Yan, M. Blue-green space cooling effect and its influencing factors in metropolitan area: A case study on the area within the Fifth Ring Road in Beijing. *Acta Ecol. Sin.* **2023**, *43*, 4904–4919. [CrossRef]
117. Yilmaz, S.; Irmak, M.A.; Qaid, A. Assessing the effects of different urban landscapes and built environment patterns on thermal comfort and air pollution in Erzurum city, Turkey. *Build. Environ.* **2022**, *219*, 109210. [CrossRef]
118. Valencia-Caballero, D.; Bouchakour, S.; Luna, A.; Garcia-Marco, B.; Huidobro, A.; Flores-Abascal, I.; Sanz, A.; Román, E. Experimental energy performance assessment of a bifacial photovoltaic system and effect of cool roof coating. *J. Build. Eng.* **2023**, *80*, 108009. [CrossRef]
119. Gradinaru, S.R.; Onose, D.A.; Oliveira, E.; Slave, A.R.; Popa, A.M.; Gavrilidis, A.A. Equity in urban greening: Evidence from strategic planning in Romania. *Landsc. Urban Plan.* **2023**, *230*, 104614. [CrossRef]
120. Li, J.; Li, C. Characterizing urban spatial structure through built form typologies: A new framework using clustering ensembles. *Land Use Policy* **2024**, *141*, 107166. [CrossRef]
121. Yang, X.; Hao, Y.; Ding, H.; Yu, C.; Liu, J.; Li, L.; Chen, J. Explainable Artificial Intelligence (XAI) framework using XGBoost and SHAP for assessing urban fire risk based on spatial distribution features. *Int. J. Disaster Risk Reduct.* **2025**, *129*, 105798. [CrossRef]
122. Wang, N.; Shen, L.; Fei, W.; Liu, Y.; Zhao, H.; Liu, L.; Wang, A.; He, B.-J. Seasonal Effects of Urban Morphology on the Thermal Environment Based on Automated Machine Learning: A Case Study of Beijing. *Remote Sens.* **2025**, *17*, 3150. [CrossRef]
123. Jing, W.; Qin, Z.; Mu, T.; Ge, Z.; Dong, Y. Evaluating thermal comfort indices for outdoor spaces on a university campus. *Sci. Rep.* **2024**, *14*, 21253. [CrossRef] [PubMed]
124. Chang, W.; Ji, X.; Wang, L.; Liu, H.; Zhang, Y.; Chen, B.; Zhou, S. A Machine-Learning Method of Predicting Vital Capacity Plateau Value for Ventilatory Pump Failure Based on Data Mining. *Healthcare* **2021**, *9*, 1306. [CrossRef]

Disclaimer/Publisher's Note: The statements, opinions and data contained in all publications are solely those of the individual author(s) and contributor(s) and not of MDPI and/or the editor(s). MDPI and/or the editor(s) disclaim responsibility for any injury to people or property resulting from any ideas, methods, instructions or products referred to in the content.